nanomaterials

MDPI

Review

Nanocrystalline Soft Magnetic Iron-Based Materials from Liquid State to Ready Product

Vladimir S. Tsepelev [1,*] and Yuri N. Starodubtsev [1,2]

[1] Research Center for Physics of Metal Liquids, Institute of New Materials and Technologies, Ural Federal University, Mira Str.19, 620002 Ekaterinburg, Russia; yunstar@mail.ru
[2] Gammamet Research and Production Enterprise, Tatishchev Str. 92, 620028 Ekaterinburg, Russia
* Correspondence: v.s.tsepelev@urfu.ru

Abstract: The review is devoted to the analysis of physical processes occurring at different stages of production and application of nanocrystalline soft magnetic materials based on Fe–Si–B doped with various chemical elements. The temperature dependences of the kinematic viscosity showed that above a critical temperature, the viscosity of multicomponent melts at the cooling stage does not coincide with the viscosity at the heating stage. Above the critical temperature, the structure of the melt is more homogeneous, the amorphous precursor from such a melt has greater plasticity and enthalpy of crystallization and, after nanocrystallization, the material has a higher permeability. The most effective inhibitor elements are insoluble in α-Fe and form a smoothed peak of heat release during crystallization. On the other hand, the finest nanograins and the highest permeability are achieved at a narrow high-temperature peak of heat release. The cluster magnetic structure of a nanocrystalline material is the cause of magnetic inhomogeneity, which affects the shape of the magnetic hysteresis loop and core losses.

Keywords: soft magnetic materials; nanocrystalline structure; liquid multicomponent alloy; grain growth inhibitor; magnetic hysteresis; magnetic core; core losses; transformer; inductive component

check for updates

Citation: Tsepelev, V.S.; Starodubtsev, Y.N. Nanocrystalline Soft Magnetic Iron-Based Materials from Liquid State to Ready Product. *Nanomaterials* **2021**, *11*, 108. https://doi.org/10.3390/nano11010108

Received: 17 November 2020
Accepted: 30 December 2020
Published: 5 January 2021

Publisher's Note: MDPI stays neutral with regard to jurisdictional claims in published maps and institutional affiliations.

Copyright: © 2021 by the authors. Licensee MDPI, Basel, Switzerland. This article is an open access article distributed under the terms and conditions of the Creative Commons Attribution (CC BY) license (https://creativecommons.org/licenses/by/4.0/).

1. Introduction

Nanocrystalline soft magnetic materials were discovered by Yoshizawa, Yamauchi and Oguma in 1986 [1,2]. This discovery was preceded by numerous research and development projects concerning amorphous soft magnetic materials. To obtain an amorphous structure, rapid quenching of the metal melt with a cooling rate of about 10^6 K·s^{-1} is used. Under industrial conditions, an amorphous ribbon 20 μm thick is produced using the planar flow casting process [3]. Amorphous Fe–B alloy, in which boron contributes to amorphization, is widely used in scientific research. For industrial purposes, the Fe–Si–B alloy [4] is more suitable, in which silicon contributes to an increase in the crystallization temperature and a decrease in the coercive force.

Crystallization of the amorphous Fe–Si–B alloy leads to the release of heat and an increase in the density, while the crystallites grow to 0.1–1 μm [5]. The first crystals are nucleated on the surface of the ribbon [6], and then the crystallization front propagates deep into the material [7]. As the grain size decreases, the length of grain boundaries increases. The grain boundaries are crystal lattice defects. Therefore, an increase in the defect density is accompanied by an increase in the coercive force of the magnetic material [8]. When the grain size decreases to 0.1 μm, the coercive force can reach several kA·m^{-1}. In the Fe–Si–B alloy, Yoshizawa and coworkers additionally introduced Cu, which has the effect of nucleation, and Nb, which increases the crystallization temperature. As a result, the Fe–Cu–Nb–Si–B alloy was obtained, which after crystallization had a crystal size significantly less than 100 nm, a coercive force of less than 1 A·m^{-1} and an initial permeability of about 100,000 [2]. This alloy with ultrafine grain structure has been named Finemet.

A decrease in the coercive force H_c in a nanocrystalline soft magnetic material is associated with a weakening of the magnetic anisotropy due to interaction of nanocrystals [9,10]. It should be taken into account that H_c is proportional to the magnetic anisotropy constant K, and the permeability μ is inversely proportional to K [11]. In a polycrystalline material, the macroscopic magnetic anisotropy coincides with the local magnetic anisotropy in each individual crystallite. This relationship is violated if the grain size is less than the magnetocrystalline exchange length:

$$L_0 \approx \sqrt{\frac{A}{|K_1|}}, \tag{1}$$

where A is the exchange constant, $J \cdot m^{-1}$, K_1 is the first constant of magnetic crystallographic anisotropy, $J \cdot m^{-3}$. The quantity L_0 compares the exchange energy with the energy of magnetic crystallographic anisotropy [12] and determines the propagation of a magnetic inhomogeneity of the domain wall type, since this quantity also determines the width of the 180° Bloch domain wall.

In the model of random magnetic anisotropy [13], the material consists of structural regions (in our case, grains) with size d, having the same exchange constant A, magnetic crystallographic anisotropy constant K_1, and saturation magnetization M_s; however, the direction of the easy magnetization axes has random distribution. A low energy of magnetic anisotropy is achieved if the magnetization in each region is oriented along the local axis of easy magnetization. However, a sharp change in the orientation of the magnetization in neighboring regions creates a large exchange energy. Therefore, within a certain length L_{ex}, which is much larger than the structural regions d, such an interconnected change in the directions of magnetization should occur, which will correspond to the minimum magnetic energy. The L_{ex} characterizes the size of the region within which the magnetizations of the structural regions correlate or interact with each other, i.e., the structural regions are connected with each other by some exchange interaction. For this reason, L_{ex} is called the exchange correlation length.

Since $L_{ex} >> d$, the fluctuations of magnetization are averaged over a large number of regions with different directions of the easy axes. In this case, in the region of volume $(L_{ex})^3$, there is always an axis of the easiest magnetization, which is determined by statistical fluctuations. It follows from statistical considerations that the magnetic anisotropy constant $\langle K \rangle$ is less than the maximum value K_1 by the square root of the number of independent contributions. Thus, the effective magnetic anisotropy constant $\langle K \rangle$ in the exchange correlation region $(L_{ex})^3$ can be written in the form [14]:

$$\langle K \rangle = \frac{K_1}{\sqrt{N}}, \tag{2}$$

where N is the number of structural regions in the volume of exchange correlation $(L_{ex})^3$. Considering that,

$$N = \left(\frac{L_{ex}}{d}\right)^3, \tag{3}$$

we obtain,

$$K = K_1 \left(\frac{d}{L_{ex}}\right)^{\frac{3}{2}}. \tag{4}$$

From a magnetic point of view, a nanocrystalline magnetic material consists of exchange correlation regions or ferromagnetic clusters. Figure 1 schematically shows the magnetic structure of a nanocrystalline alloy [15]. Individual crystal grains of size d with the magnetic anisotropy constant K_1 have random directed easy magnetization axes, indicated by black arrows. Ferromagnetic clusters have the size L_{ex}, the effective magnetic anisotropy constant $\langle K \rangle$, and the easiest magnetization axes, indicated by double arrows.

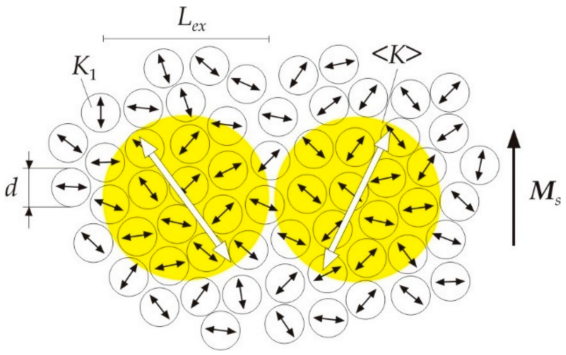

Figure 1. Schematic representation of the magnetic structure of a nanocrystalline soft magnetic alloy. Adapted from [15].

The exchange correlation length L_{ex} can be found from the condition for the minimum magnetic energy density of the ferromagnet, which is the sum of the magnetic anisotropy energy density [13]:

$$E_{ma} = -\langle K \rangle \tag{5}$$

and exchange energy density,

$$E_{ex} \approx \frac{A}{L_{ex}^2}. \tag{6}$$

From (4)–(6) it follows that magnetic energy of a ferromagnet is minimal at:

$$L_{ex} \approx \frac{A^2}{K_1^2 d^3}. \tag{7}$$

After substituting L_{ex} in (4), we obtain the effective magnetic anisotropy constant $\langle K \rangle$ in the form:

$$\langle K \rangle = \frac{K_1^4 d^6}{A^3} = K_1 \left(\frac{d}{L_0} \right)^6. \tag{8}$$

Thus, the effective magnetic anisotropy constant $\langle K \rangle$ depends on the grain size as d^6. The exponent approaches 3 in the presence of a strong induced magnetic anisotropy [16] or in the presence of a grain size distribution [17,18].

In a nanocrystalline alloy, the structural region is a crystal grain. For nanocrystals of the $Fe_{80}Si_{20}$ solid solution, the magnetic anisotropy constant K_1 is 8×10^3 J·m^{-3} and the exchange constant A is 10^{-11} J·m^{-1}. After substituting these values in (1), we obtain the magnetocrystalline exchange length L_0 = 35 nm. Figure 2 shows the dependence of the effective magnetic anisotropy constant $\langle K \rangle$ on the grain size d for L_0 = 35·nm in accordance with formula (8) [19] (pp. 240–244). At a grain size of 10 nm, the effective constant $\langle K \rangle$ decreases by about 2000 times as compared with the magnetic crystallographic constant K_1.

From formula (7) for a grain size d = 10 nm, we calculate the size of the ferromagnetic cluster L_{ex}, which is of the order of 1 μm. Thus, about 100 nanograins are located along the diameter of the α-$Fe_{80}Si_{20}$ ferromagnetic cluster. From formulas (7) and (8), we obtain the following expression for the size of a ferromagnetic cluster:

$$L_{ex} \approx \sqrt{\frac{A}{\langle K \rangle}}. \tag{9}$$

Consequently, with a decrease in the effective magnetic anisotropy constant $\langle K \rangle$, the size of ferromagnetic clusters L_{ex} will increase.

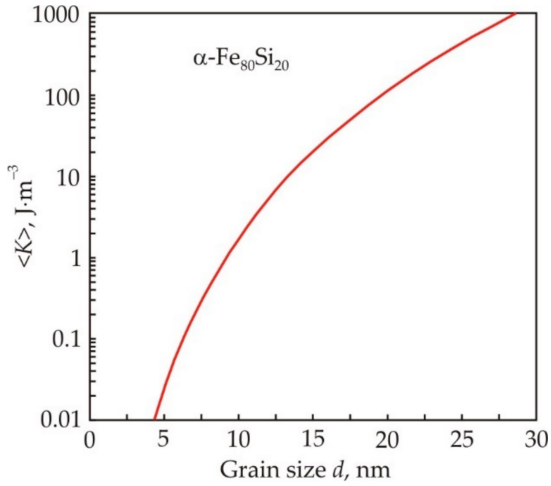

Figure 2. Dependence of the effective magnetic anisotropy constant $\langle K \rangle$ on the grain size d in the α-$Fe_{80}Si_{20}$ alloy, obtained in the random anisotropy model. Reproduced with permission from [19] (pp. 240–244).

The production of magnetic systems from nanocrystalline materials can be divided into several technological operations [19] (pp. 244–249). The initial operation is the smelting of an alloy with a given chemical composition. The next step is rapid quenching of the melt, resulting in an amorphous precursor in the form of a 20 μm thick ribbon. Heat treatment of the amorphous precursor ensures the formation of a nanocrystalline structure with a guaranteed level of magnetic properties. As a rule, magnetic circuits or cores are first made from an amorphous precursor, and then they are subjected to heat treatment. Heat is released during crystallization, so the optimal heat treatment depends not only on the chemical composition of the alloy, but also on the size of the cores.

The purpose of this review is to analyze the physical processes occurring at different stages of the production and application of nanocrystalline soft magnetic materials. The object was Fe–Si–B alloys doped with various chemical elements, which have found wide practical application. The section "Multicomponent melts" analyzes the effect of temperature and chemical composition of melts on the structure of an amorphous precursor and nanocrystalline alloy. The section "Nanocrystallization" discusses the main features of nanocrystallization, and "Grain growth inhibitors" evaluates the effectiveness of using inhibitors to achieve the optimal nanocrystalline structure. The section "Solute elements in α-Fe" analyzes the effect of Ni, Co, Si, Al soluble in nanocrystals on magnetic properties. The "Core losses" section contains an analysis of magnetic losses, which play a critical role in various applications of soft magnetic materials. The last section compares the magnetic properties of various nanocrystalline soft magnetic materials and analyzes their application in power electronics.

2. Multicomponent Melts

Nanocrystalline soft magnetic materials are multicomponent alloys, for example, Finemet has the composition $Fe_{73.5}Cu_1Nb_3Si_{13.5}B_9$ [2]. In Fe–Si–B-based alloys, there is a strong covalent bond in Fe–B and Fe–Si, both in the amorphous and in the liquid states, and the B and Si atoms interact weakly [20]. A non-uniform distribution of atoms takes place in the melt [21]. The tendency for different atoms to approach each other leads to the formation of clusters with a structure close to Fe_3B and Fe_2B [22,23], as well as Fe_3Si and FeSi [24,25], and boron-based clusters are formed more easily [26]. The inhomogeneous structure of metal melts manifests itself in the features of the temperature dependences of physical properties.

Among the physical properties, viscosity most reflects the structure of melts. Kinematic viscosity ν, $m^2 \cdot s^{-1}$, must correspond to the equation [27]:

$$\nu = \nu_0 e^{\frac{E_a}{RT}}, \quad (10)$$

where T is the absolute temperature, K, ν_0 is a pre-exponential factor with the dimension of the kinematic viscosity $m^2 \cdot s^{-1}$, E_a is the activation energy of the viscous flow, $J \cdot mol^{-1}$, R is the gas constant, $J \cdot K^{-1} \cdot mol^{-1}$. At constant ν_0 and E_a, the melt viscosity decreases with increasing temperature according to Equation (10). After taking the logarithm we obtain:

$$\ln \nu = \ln \nu_0 + \frac{E_a}{RT}. \quad (11)$$

Thus, the logarithm of the kinematic viscosity is a linear function of the inverse absolute temperature. This representation allows one to calculate the pre-exponential factor ν_0 and the activation energy E_a from the temperature dependence of the viscosity, in which the viscosity is presented on a logarithmic scale, and the absolute temperature is in the inverse scale.

Figure 3 shows the kinematic viscosity in logarithmic scale and absolute temperature in the inverse scale for two alloys $Fe_{72.5}Cu_1Nb_2Mo_{1.5}Si_{14}B_9$ (a) and $Fe_{84.5}Cu_{0.6}Nb_{0.5}Si_{1.5}B_{8.6}P_4C_{0.3}$ (b), which have significantly different silicon contents. In accordance with Equation (11), the temperature dependences of viscosity should represent a straight line, but in multicomponent melts they have a number of characteristic features [28]. When the melt is heated above a certain temperature T_h, the cooling curve coincides with the heating curve at $T > T_h$ and deviates at $T < T_h$. In this case, there is a temperature region near T_h, within which the heating and cooling curves form a hysteresis loop. For these reasons, the temperature T_h can be called the hysteresis temperature or branching temperature T_{br} [29].

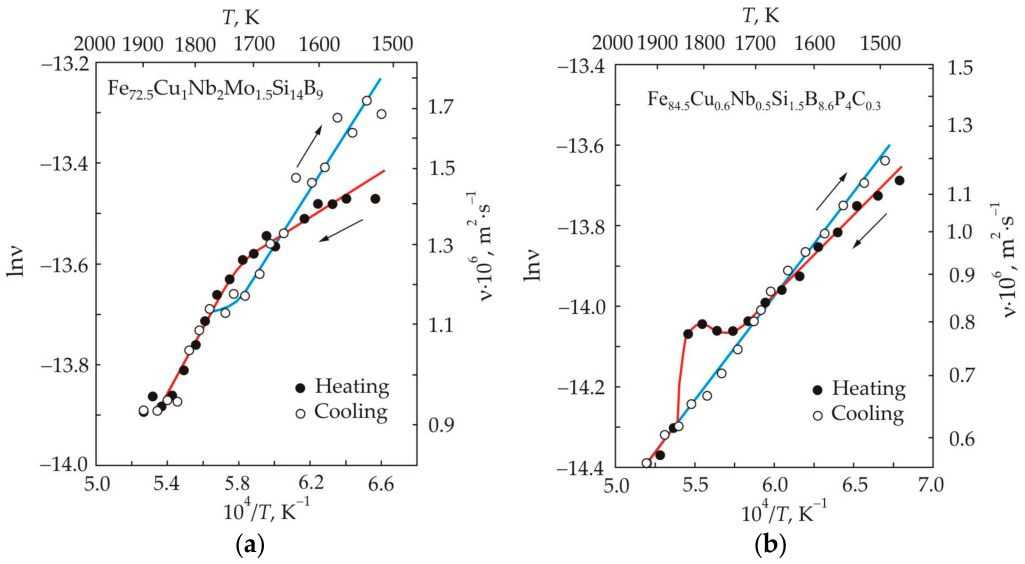

Figure 3. Temperature dependences of kinematic viscosity ν for nanocrystalline alloys $Fe_{72.5}Cu_1Nb_2Mo_{1.5}Si_{14}B_9$ (**a**) and $Fe_{84.5}Cu_{0.6}Nb_{0.5}Si_{1.5}B_{8.6}P_4C_{0.3}$ (**b**). The arrows show the direction of temperature change.

The greatest nonlinearity of the temperature dependence of viscosity in logarithmic and inverse scales is observed during heating. The temperature at which the activation energy in the $Fe_{72.5}Cu_1Nb_2Mo_{1.5}Si_{14}B_9$ melt changes can be called the critical temperature T_k, see Figure 3a. This temperature corresponds approximately to the middle of the temperature range for the hysteresis loop. Another type of anomaly manifests itself in the form of a local increase in viscosity, as for the $Fe_{84.5}Cu_{0.6}Nb_{0.5}Si_{1.5}B_{8.6}P_4C_{0.3}$ melt in Figure 3b. The critical temperature is associated with the rearrangement of the melt structure. In

particular, in the high-temperature region, the formation of a more homogeneous structure occurs due to the dissolution of clusters; therefore, this temperature is sometimes called dissolution temperature T_d [29]. At the cooling stage, the non-linearity of the temperature dependence of viscosity is less pronounced or completely absent.

In binary melts Fe-Si [25] and Fe-B [30], the temperature dependences of the kinematic viscosity were obtained, which were similar to those for the $Fe_{72.5}Cu_1Nb_2Mo_{1.5}Si_{14}B_9$ and $Fe_{84.5}Cu_{0.6}Nb_{0.5}Si_{1.5}B_{8.6}P_4C_{0.3}$ melts. The viscosity of the Fe-Si melt varied smoothly during heating and cooling. An anomaly was observed in the Fe-B melt, which manifested itself in a local increase in viscosity near the critical temperature. The appearance of the anomaly in boron-containing melts was associated with the rearrangement of FeB- and Fe_2B-based clusters, which transform with increasing temperature into Fe_4B- [30] or Fe_3B-based clusters [31]. A local increase in viscosity near the critical temperature is not observed in the $Fe_{72.5}Cu_1Nb_2Mo_{1.5}Si_{14}B_9$ melt. In addition to B, this alloy also contains a large amount of Si. Apparently, in the presence of silicon, a significant part of boron is bound to less stable B–Si and Fe–B–Si compounds [32].

Long time exposure of the melt at a fixed temperature is accompanied by fluctuations in viscosity, the amplitude of which significantly exceeds the measurement error [33]. The greatest temporal instability of the melt is observed at the temperature of structural transformations [34]. The reason for the oscillations can be a transition from a non-equilibrium melt structure inherited from the initial crystalline phases to an equilibrium state, or random oscillations associated with the periodic appearance and destruction of cluster structures, or an intense structural transformation of the melt [35].

Figure 4 shows the kinematic viscosity in logarithmic scale and absolute temperature in the inverse scale for $Fe_{73.5}Cu_1M_3Si_{13.5}B_9$ melts with different inhibitors M = Nb, Mo, V, Cr at the stage of heating (a) and cooling (b) [36]. At the heating stage, the temperature dependences of melts with Nb, Mo, and V have two linear sections, the slope of which changes at the critical temperature T_k = 1770 K. In a melt with Nb, the activation energy increases upon going to the high-temperature region. This pattern is also observed in the $Fe_{72.5}Cu_1Nb_2Mo_{1.5}Si_{14}B_9$ melt, which is dominated by Nb, see Figure 3a. In melts with Mo and V, the activation energy decreases during the transition to the high-temperature region. In a melt with Cr in the entire temperature range, the dependence is a straight line. At the cooling stage, linear dependences were obtained in the entire temperature range for all melts.

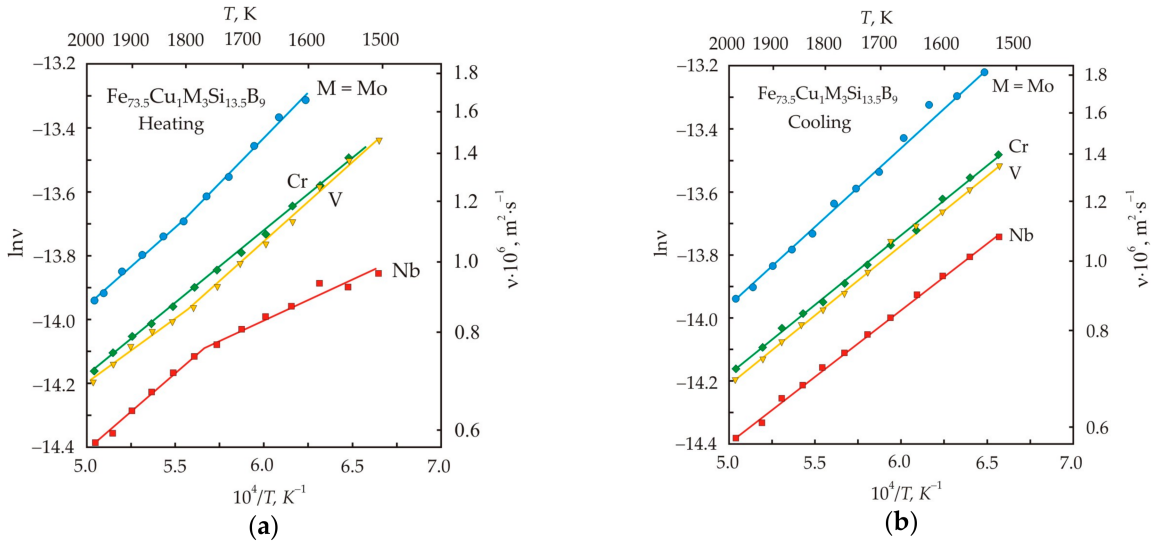

Figure 4. Temperature dependences of the kinematic viscosity ν for nanocrystalline $Fe_{73.5}Cu_1M_3Si_{13.5}B_9$ alloys with different inhibitors M = Nb, Mo, V, Cr at the stage of heating (**a**) and cooling (**b**). Reproduced with permission from [36].

Table 1 shows the calculated values of the activation energy E_a for melts with various inhibitors [36]. In the low-temperature region, a melt with Nb has the lowest E_a = 21 kJ·mol^{-1}, and a melt with Mo has the highest one, E_a = 47 kJ·mol^{-1}. In the high-temperature region at the stages of heating and cooling, the activation energies of melts differ insignificantly. Since after cooling the viscosity of the melts does not recover to its initial value, it can be concluded that the melt underwent irreversible changes.

Table 1. Activation energy of viscous flow for $Fe_{73.5}Cu_1M_3Si_{13.5}B_9$ melts with different inhibitors M = Nb, Mo, V, Cr. Reproduced with permission from [36].

Inhibitors, M	Activation Energy E_a, kJ·mol^{-1}			
	Heating		Cooling	
	T < 1770 K	T > 1770 K	T < 1770 K	T > 1770 K
Nb	21	42	35	35
Mo	47	41	41	41
V	43	34	36	36
Cr	38	38	40	40

The viscosity of $Fe_{73.5}Cu_1M_3Si_{13.5}B_9$ melts with various inhibitors correlates well with the free volume [36]. The Nb melt has the largest free volume, while the Mo melt has the smallest. The metallic radius of Nb, Mo, V, Cr, and Fe is 146, 139, 134, 128, and 126 pm, respectively [37]. At a temperature of 1000 K, Nb is slightly soluble in α-Fe, and the solubility of other elements increases with decreasing atomic size. Atoms of inhibitory elements occupy vacant positions in a substitutional solid solution. A large atomic radius favors the formation of vacancies [38], which are concentrated near inhibitory atoms with the formation of vacancy clusters [39]. Consequently, an alloy containing Nb should have the highest concentration of vacancies already before the onset of melting. A high concentration of vacancies should facilitate easier activation of the viscous flow.

At the stage of melting, the melt retains the short-range order structure inherited from the multiphase solid state. In this case, the structural component of the melt is clusters, the size of which depends on the temperature [40]. As the temperature increases, the cluster size decreases, and at temperatures above T_k, the melt structure becomes more homogeneous. If the melt is heated above the critical temperature and then quickly transferred to an amorphous solid state, then it can be expected that the homogeneous structure of the liquid will remain in the amorphous state. The heredity of the structure was investigated on samples of amorphous ribbon, which was obtained after heating the melt above and below the critical temperature. After high-temperature holding of melt, an amorphous ribbon has a lower ordering of atoms [41], a larger molar volume [42], greater plasticity [41,43], hardness and fracture toughness [43], and a higher enthalpy of crystallization [42,44]. Thus, the heredity of the melt structure remains in the amorphous solid state after melt quenching.

For the study of melts, an ingot is usually used, which was obtained after melting the alloy and slow cooling. The melt viscosity depends on its prehistory. Therefore, it should be expected that the structure and properties of the melt from the amorphous precursor will be different. When choosing the temperature regime, it was taken into account that the $Fe_{72,5}Cu_1Nb_2Mo_{1,5}Si_{14}B_9$ alloy has a critical temperature of 1760 K. The melt was heated to 1795 K, i.e., above the critical temperature, kept at this temperature for 5 min, then cooled to 1750 K, held for another 5 min and then the melt was quickly quenched. This mode of obtaining an amorphous precursor and a melt from this amorphous ribbon will be called "overheated". In the "not overheated" mode, the melt was heated to 1750 K, i.e., below the critical temperature, kept at this temperature for 5 min, and then the melt was quickly quenched.

Figure 5 shows the temperature dependences of the kinematic viscosity at the first heating–cooling cycle and at the second heating of the melt obtained from the amorphous

$Fe_{72,5}Cu_1Nb_2Mo_{1,5}Si_{14}B_9$ ribbon [45]. It follows from the figure that immediately after the melting of the amorphous ribbon, the viscosity of the overheated and not overheated melts is almost the same. However, after increasing the temperature to about 1540 K, the curves diverge significantly. The viscosity of the overheated melt goes up sharply, while the viscosity of the not overheated melt changes insignificantly. At temperatures above 1540 K, the viscosity decreases in accordance with the classical concept of the free volume [46,47].

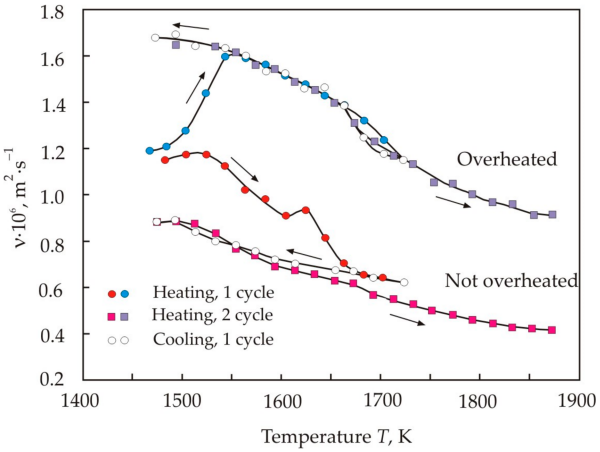

Figure 5. Temperature dependences of kinematic viscosity ν for the first heating–cooling cycle and for the second heating in the overheated and not overheated melts prepared from the amorphous $Fe_{72.5}Cu_1Nb_2Mo_{1.5}Si_{14}B_9$ ribbon. The arrows show the direction of temperature change [45].

The temperature curve of the viscosity of the overheated melt reaches a stable trajectory already at the second heating, with the exception of a small loop in the range of 1670–1720 K. In the not overheated melt, the trajectory of viscosity continued to decrease. From Figure 5, we can conclude that the melt obtained from the amorphous ribbon is non-equilibrium, and the not overheated melt has the greatest deviation from the equilibrium structure. The difference in the viscosity indicates a different structure of atomic groups participating in the viscous flow.

In the hard spheres model, the viscosity of the melt can be represented as [48]:

$$\nu \propto a\sqrt{\frac{k_B T}{m}}, \tag{12}$$

where a is the atomic size, m, m is the atomic mass, kg, $k_B = 1.38 \times 10{-}23\ \mathrm{J{\cdot}K^{-1}}$ is Boltzmann constant. If clusters are involved in a viscous flow, then it should be taken into account that the cluster mass is proportional to the number of atoms in the cluster, and the cluster size is not proportional [49]. Figure 6 shows the dependence of the relative viscosity of the melt $\nu c/\nu$, where νc is the viscosity of a liquid consisting of clusters on the number of atoms in the cluster n [45]. It follows from the Figure that the viscosity of the liquid should decrease with increasing cluster size. The same conclusion can be obtained on the basis of general concepts [28], since as the cluster size decreases, the energy of interaction between them increases, and this should lead to an increase in the viscosity.

When the amorphous ribbon is heated, crystallization and melting processes take place. At the first stage of crystallization, nanocrystalline grains are formed with an average size of about 10 nm [50]. It is important that in an amorphous ribbon prepared from an overheated melt, there are noticeably more small grains 1–2 nm in size [44]. At the second stage of crystallization, metastable phases based on Fe–B and Fe–Si are formed [51], while Fe–B, Fe–Nb, and Nb–B clusters dominate in the melt [52]. Apparently, the finer nanocrystalline structure in the superheated ribbon became the basis for the formation of a finely dispersed melt structure. This makes it possible to associate the increased viscosity of the superheated melt with the small size of atomic groups in the liquid.

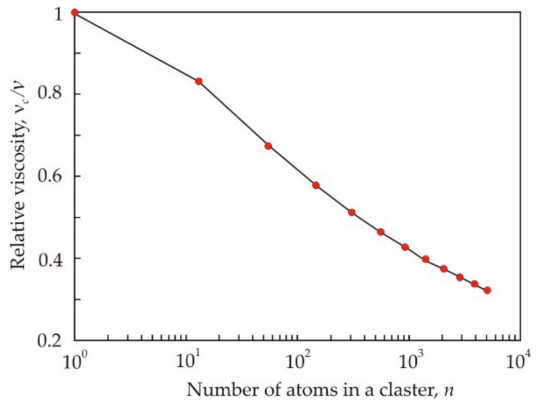

Figure 6. The dependence of relative melt viscosity ν_c/ν on the number of atoms in a cluster n [45].

Figure 7 shows that in the third heating–cooling cycle, a good stabilization of the trajectories of the viscosity curves was achieved [45]. Despite this, in the region of the critical temperature, irreversibility remains, and it manifests itself in the form of a hysteresis loop. The branching of the curves begins at a temperature of 1670 K. Moreover, in this region there is also an increased slope of the curves, which indicates an increase in the activation energy of the viscous flow. The calculation results for the activation energy E_a and pre-exponential factor ν_0 are presented in Table 2 [45]. The entire temperature range was divided into intervals with different activation energies. The calculated values were obtained by linear extrapolation of the experimental points for each temperature range.

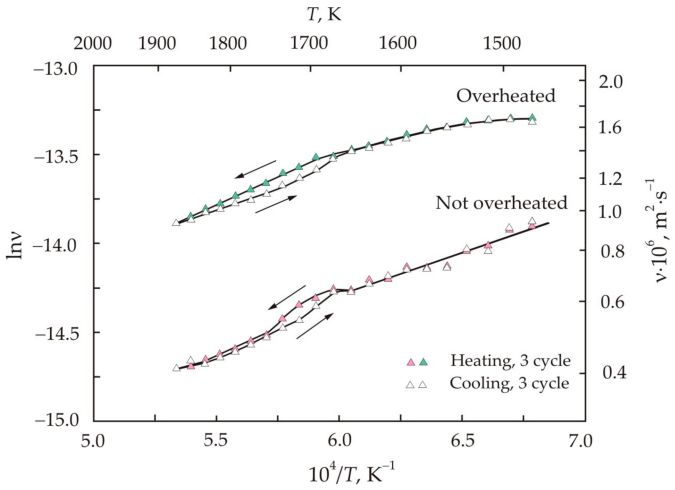

Figure 7. Temperature dependences of kinematic viscosity ν for the third heating—cooling cycle in the overheated and not overheated melt prepared from the amorphous $Fe_{72.5}Cu_1Nb_2Mo_{1.5}Si_{14}B_9$ ribbon. The arrows show the direction of temperature change [45].

Table 2. The activation energy E_a, cluster size d, and pre-exponential factor ν_0 in the overheated and not overheated melt obtained from the amorphous $Fe_{72.5}Cu_1Nb_2Mo_{1.5}Si_{14}B_9$ ribbon [45].

Temperature Range	Heating			Cooling		
	E_a, kJ·mol^{-1}	$\nu_0 \cdot 10^8$,·m^2·s^{-1}	d, nm	E_a, kJ·mol^{-1}	$\nu_0 \cdot 10^8$,·m^2·s^{-1}	d, nm
Overheated melt						
1470–1670 K	23.2	26.3	0.05	26.0	21.1	0.05
1670–1870 K	51.4	3.47	2.5	45.7	4.8	1.5
Not overheated melt						
1470–1670 K	37.6	7.6	0.4	38.2	4.0	1.5
1670–1750 K	83.1	0.27	380	76.1	0.26	410
1750–1870 K	44.1	2.31	6	38.4	3.47	2.5

Table 2 also shows the calculated cluster sizes d. The calculation was carried out using the Eyring model based on the transition state theory [47]. In the Eyring model, the viscosity can be represented as [53]:

$$\nu = \left(\frac{2\pi k_B T}{\rho}\right)^{\frac{1}{2}} \left(\frac{v_f}{v}\right)^{\frac{1}{3}} d^{\frac{-1}{2}} e^{\frac{E_a}{RT}}, \quad (13)$$

where ρ is the melt density, kg·m^{-3}, d is the particle diameter, m, v is the volume occupied by one particle, m^3, v_f is the free volume of liquid, m^3, v_f/v is the relative free volume. From formula (13), it follows that the melt viscosity decreases with increasing particle size. Comparing Equations (10) and (13), we obtain:

$$d = \left(\frac{2\pi k_B T}{\rho}\right) \left(\frac{v_f}{v}\right)^{\frac{2}{3}} \nu_0^{-2}. \quad (14)$$

To calculate the cluster size, we used the measured density and free volume of melts [36,53].

When discussing the data on the cluster size, it is necessary to take into account that the model concepts differ from a real multicomponent liquid, in which atoms and clusters of different compositions and sizes coexist. For the low-temperature region in the overheated regime, the effective cluster size of 0.05 nm was obtained, which can be taken as the atomic size, taking into account the accuracy of model representations. Thus, in the low-temperature region, the viscosity of the melt is associated with the vibrations of individual atoms, which are mainly located near their equilibrium positions. With increasing temperature, the mobility of atoms increases, but strong bonds Fe–B, Fe–Nb(Mo), and Nb(Mo)–B restrain decomposition into individual atoms and ensure the formation of clusters.

Table 2 shows that the cluster size is higher in the not overheated melt, which also has a lower viscosity. The largest cluster size falls on the region of the hysteresis loop, where the activation energy is also the highest. Table 2 also shows that the cluster size and activation energy are related. The dependence of the activation energy E_a on the cluster size d is shown in Figure 8. This relationship can be written as a linear function:

$$E_a = a + b \ln d, \quad (15)$$

which has an adjusted coefficient of determination $R^2_{adj} = 0.93$. In formula (15), $a = 170{,}000$ J·mol^{-1} and $b = 6300$ J·mol^{-1}, and the activation energy and the cluster size have the dimensions J·mol^{-1} and m, respectively. The quantity b characterizes the change in the activation energy per unit cluster size on a logarithmic scale. formula (15) can be transformed to the form:

$$d = 1.76 \times 10^{-12} e^{\frac{E_a}{b}}, \quad (16)$$

which expresses the dependence of the cluster size on the activation energy.

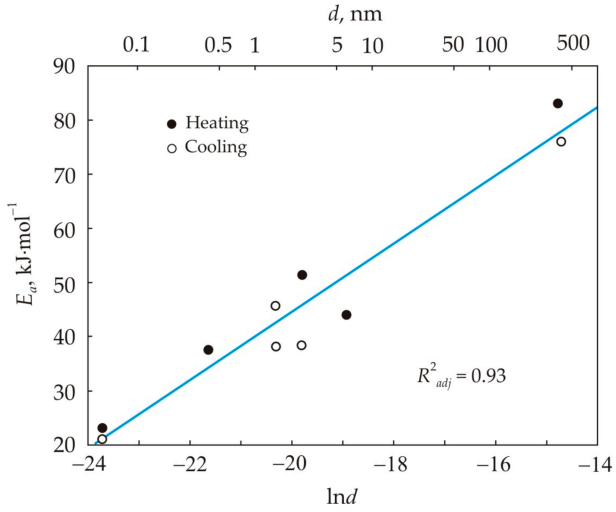

Figure 8. Relationship between the activation energy of viscous flow E_a and the cluster size d.

The study of multicomponent melts shows that the structures of the liquid and solid states are interrelated. The melt heated above the critical temperature has the most homogeneous structure. An amorphous precursor obtained from a homogeneous melt has high plasticity and hardness, as well as the enthalpy of crystallization. After nanocrystallization of an amorphous precursor from a overheated melt, a magnetic material with a higher permeability was obtained [44].

3. Nanocrystallization

The main stage in the production of nanocrystalline soft magnetic materials is the heat treatment of the amorphous precursor, as a result of which a nanocrystalline structure is formed. The iron-based alloy $Fe_{73.5}Cu_1Nb_3Si_{13.5}B_9$, which is associated with the Finemet brand, was the first nanocrystalline soft magnetic material with high permeability. At present, this alloy with slight variations in chemical composition is the basis for the production of nanocrystalline soft magnetic materials. At the initial stage of heat treatment, copper-rich clusters are formed, which create a chemical inhomogeneity of the amorphous matrix. These inhomogeneities are centers of heterogeneous nucleation of a large number of α-FeSi crystals throughout the material volume [54–56]. Niobium inhibits the growth of the crystalline phase to a higher temperature and also prevents the formation of iron borides [57,58].

Figure 9 schematically shows the different stages of nanocrystallization of the Finemet alloy [59]. At the stage of heterogeneous nucleation, crystals of the α-FeSi solid solution are formed, in which the silicon content is lower than its nominal value in the amorphous state [59]. With time, silicon diffuses into the crystalline phase and the silicon content in the solid solution increases to 20 at. % [59,60]. At the final stage of nanocrystallization, grains are formed, the composition of which is close to $Fe_{80}Si_{20}$ and Fe_3Si, surrounded by a residual amorphous matrix. The volume fraction of the crystalline phase is about 0.7 [15].

Figure 10 shows the diffraction patterns of the $Fe_{72.5}Cu_1Nb_2Mo_{1.5}Si_{14}B_9$ alloy during heating with a step of 25 K [61]. At temperatures below 725 K, the diffraction patterns have the form of halos, which correspond to the amorphous state. The first appearance of a small reflection at a larger angle 2θ coincides with the onset of crystallization at a temperature of 725 K. With increasing temperature, the halo is replaced by a set of individual reflections {110}, {200}, which correspond to the bcc lattice.

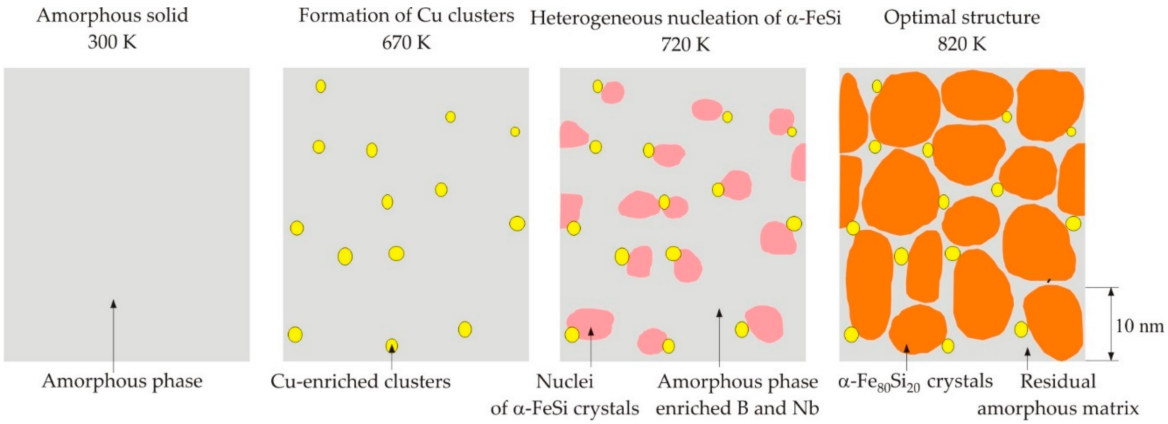

Figure 9. Different stages of the formation of a nanocrystalline structure in the $Fe_{73.5}Cu_1Nb_3Si_{13.5}B_9$ alloy. Adapted from [59].

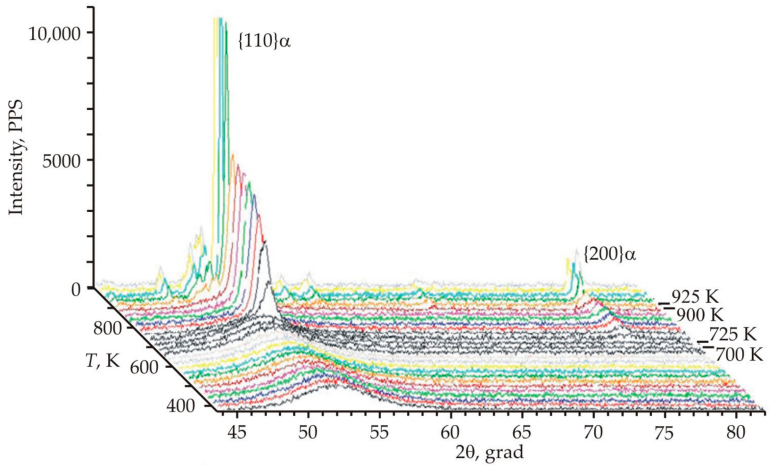

Figure 10. Diffraction patterns of the $Fe_{72.5}Cu_1Nb_2Mo_{1.5}Si_{14}B_9$ alloy during heating [61].

At a temperature of 880 K, boride and intermetallic phases are found. A sharp increase in the height of the peaks with a simultaneous decrease in their width was recorded at a temperature of 925 K. This indicates a sharp increase in the degree of perfection of the crystal lattice, which can be associated with recrystallization and grain coarsening. An intense release of energy 386 and 88 $kJ \cdot mol^{-1}$ occurs at temperatures of 815 and 950 K and this corresponds to the peaks of crystallization and recrystallization.

Figure 11 shows the change in time of the temperature and permeability of the cores made of $Fe_{72.5}Cu_1Nb_2Mo_{1.5}Si_{14}B_9$ and $Fe_{73.5}Cu_1Nb_2Mo_{1.5}Si_{16}B_6$ alloys during nanocrystallization in a furnace with a constant temperature of 813 K [50]. To fix the structure at different stages of crystallization, the cores were taken out of the furnace and quickly cooled in the time indicated by the dots in Figure 11. The peak temperature in the core indicates the release of heat during the crystallization process. The higher Si content in the $Fe_{73.5}Cu_1Nb_2Mo_{1.5}Si_{16}B_6$ alloy increases the enthalpy of crystallization [62]. Therefore, this alloy has a higher heating rate and the peak temperature T_{max}.

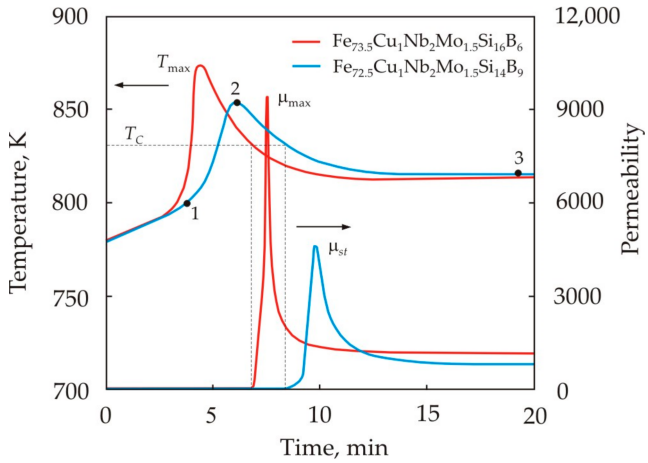

Figure 11. The change in time of the temperature and permeability of the cores made of $Fe_{72.5}Cu_1Nb_2Mo_{1.5}Si_{14}B_9$ and $Fe_{73.5}Cu_1Nb_2Mo_{1.5}Si_{16}B_6$ alloys during nanocrystallization in a furnace with a constant temperature of 813 K. Adapted from [50].

The peak of permeability coincides with the formation of a ferromagnetic state in nanocrystals at the cooling stage. Figure 11 shows that the Curie temperature of the primary crystalline phase is the same for alloys with different silicon contents. After reaching the peak value μ_{max}, the permeability decreases rather quickly, stabilizing at the level of μ_{st} [50,63]. By that time, the diffusion of chemical elements, as well as the residual movement of grain boundaries, still continues. Near the Curie point, the magnetic anisotropy constant of the crystalline phase is low. Therefore, the permeability is high enough, despite the fact that the crystals are surrounded by a non-magnetic amorphous matrix. Due to the diffusion of silicon, the chemical composition of the crystalline and amorphous phases changes over time. The stabilization of the chemical composition, as well as the occupation of stable positions by the diffusing atoms at the sites of the crystal lattice, leads to a decrease and stabilization of the permeability.

The structure of sample 1 in Figure 11 represents an amorphous matrix with a small fraction of grains, the average size of which is 6 nm [50]. The maximum frequency distribution falls on grains 2 nm in size, which can be identified as nuclei of the crystalline phase. The structures of samples 2 and 3 practically do not differ with an average grain size of 10 nm. After cooling, sample 1 had an initial permeability $\mu_{0.08}$ = 5600 and a coercive force H_c = 1.25 A/m, while in samples 2 and 3 the magnetic properties were the same, $\mu_{0.08}$ = 70,000 иH_c = 0.50 A/m.

Figure 12 shows the dependences of the initial permeability $\mu_{0.08}$, the coercive force H_c and the remanence ratio B_r/B_{800} on the annealing temperature T_a of the $Fe_{72.5}Cu_1Nb_2Mo_{1.5}Si_{14}B_9$ alloy being held at a fixed temperature for 1 h [64]. It follows from the Figure that the remanence ratio decreases almost linearly with increasing temperature, and the initial permeability $\mu_{0.08}$ and the coercive force H_c have an optimal temperature range. To obtain a high initial permeability, the optimum annealing temperature should be approximately 20 K higher than the minimum coercive force. High or low remanence ratio B_r/B_{800} distinguishes low-temperature and high-temperature annealing of nanocrystalline soft magnetic alloy.

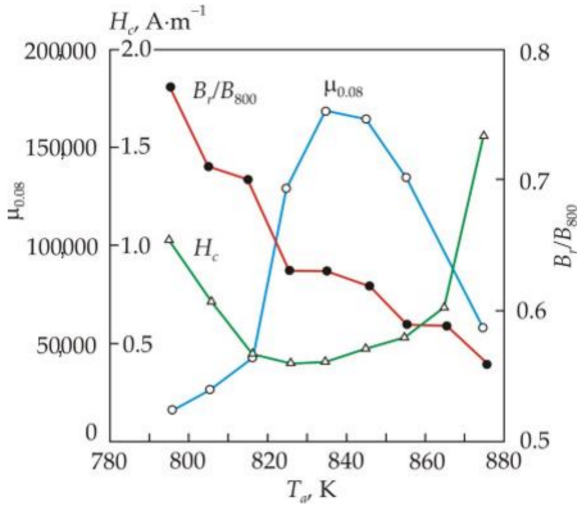

Figure 12. Dependences of the initial permeability $\mu_{0.08}$, coercive force H_c, and remanence ratio B_r/B_{800} on the annealing temperature T_a of the $Fe_{72.5}Cu_1Nb_2Mo_{1.5}Si_{14}B_9$ alloy. Adapted from [64].

Figure 13 shows the dependences of the relative magnetic susceptibility χ_T/χ_{300} of a ribbon made of the $Fe_{72.5}Cu_1Nb_2Mo_{1.5}Si_{14}B_9$ alloy on temperature during heating and cooling [65]. The arrows in the figure indicate the Curie points of crystalline phases, which are precipitated during crystallization [66–69]. A sharp drop in the magnetic susceptibility during heating at a temperature of 575 K corresponds to the Curie point of the alloy in the amorphous state. The increase in susceptibility at a temperature of 820 K is associated with the appearance of ferromagnetism in the crystals of the α-FeSi solid solution. The maximum magnetic susceptibility occurs at a temperature of 840 K, which corresponds to the maximum volume of the crystalline ferromagnetic phase. The temperature 862 K, at which the relative magnetic susceptibility approaches zero, is close to the Curie point of the $Fe_{80}Si_{20}$ solid solution [66]. With an increase in temperature to 970 K, further structural transformations occur and they are associated with the crystallization of the residual amorphous phase and the growth of the crystal grain [70].

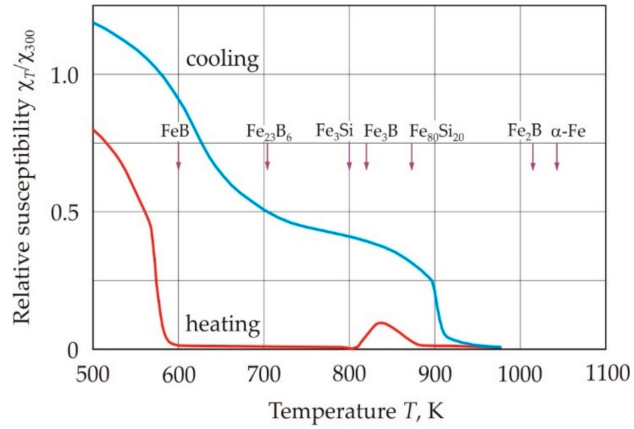

Figure 13. Temperature dependence of the relative magnetic susceptibility χ_T/χ_{300} of a ribbon made of the $Fe_{72.5}Cu_1Nb_2Mo_{1.5}Si_{14}B_9$ alloy during heating and cooling and the Curie point of crystalline phases. Reproduced with permission from [65].

At the cooling stage, at a temperature of 910 K, an increase in the magnetic susceptibility is observed, which provides the Fe–Si crystalline phase, see Figure 13. The higher Curie point of this phase in comparison with $Fe_{80}Si_{20}$ is due to the reduced silicon content in Fe–Si crystals after recrystallization at temperatures above 900 K [71]. The second rise in

the magnetic susceptibility at a temperature of 700 K can be associated with the appearance of ferromagnetism in a phase with a composition close to $Fe_{23}B_6$.

Heat treatment of a nanocrystalline alloy is accompanied by a change in its dimensions associated with structural transformations. Figure 14 shows the relative change in the length Δ of a ribbon made of the $Fe_{72.5}Cu_1Nb_2Mo_{1.5}Si_{14}B_9$ alloy as a function of temperature T during heating and cooling [65]. On the heating curve up to a temperature of 720 K, the length of the ribbon grows almost linearly with the coefficient of linear thermal expansion $\alpha_L = 8 \times 10^{-6}\ K^{-1}$. A small area at a temperature of 450–500 K coincides with the onset of structural relaxation of the amorphous precursor [72,73]. An increase in temperature to 820 K leads to a sharp reduction in the length of the ribbon with the coefficient $\alpha_L = -30 \times 10^{-6}\ K^{-1}$, which is due to crystallization. The characteristic minimum on the heating curve in the region of 860 K corresponds to the end of the crystallization.

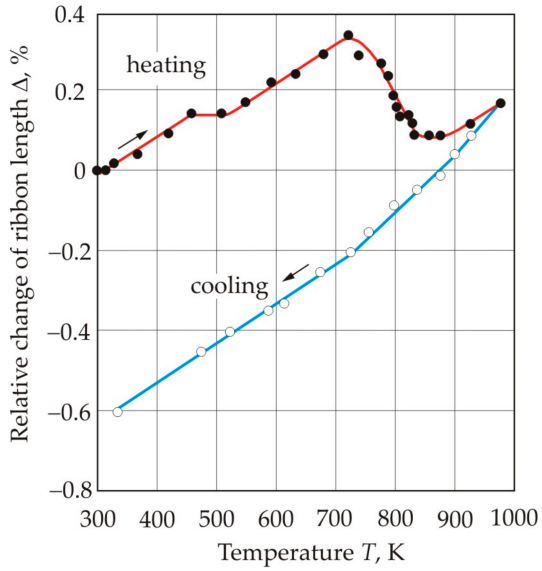

Figure 14. Relative change in the length Δ of a ribbon from the $Fe_{72.5}Cu_1Nb_2Mo_{1.5}Si_{14}B_9$ alloy as a function of temperature T during heating and cooling. Reproduced with permission from [65].

During the cooling, the curve of the length change does not follow the heating curve, even in the high temperature region. This is obvious, since during heating, structural transformations occur continuously, and after they are fixed at the maximum temperature, the structure does not change. Three linear sections can be distinguished on the cooling curve, and the slope of the curves changes at approximately 900 and 700 K. With a decrease in temperature, the coefficient of linear thermal expansion gradually decreases: $18{\cdot}10^{-6}$, 13×10^{-6} и$10 \times 10^{-6}\ K^{-1}$. The change in the slope of the curves occurs at a temperatures at which the magnetic state of the sample changes in accordance with the cooling curve in Figure 13. Above 900 K, the paramagnetic phase predominates. With a decrease in temperature, the ferromagnetic properties of the Fe-Si crystalline phase appear. At temperatures below 700 K, the crystalline phase of $Fe_{23}B_6$ becomes ferromagnetic. Thus, the magnetic state of the nanocrystalline alloy has a significant effect on the coefficient of linear thermal expansion of the material.

4. Grain Growth Inhibitors

Grain growth inhibitors can be arranged in the sequence Cr, V, W = Mo, Nb = Ta, Zr, in which each successive element leads to an increase in the crystallization temperature, a decrease in the grain size, and an increase in the permeability of the nanocrystalline alloy [74–76]. The crystallization process in alloys containing different inhibitors is very different. Figure 15 shows the change in time of the temperature of $Fe_{73.5}Cu_1M_3Si_{13.5}B_9$ cores, where M = Nb, W, V, during crystallization in a furnace with a fixed temperature

T_a = 823 K [77]. Crystallization in the alloy with Nb has the lowest peak temperature T_{max} = 840 K, the heating rate V_{max} = 15 K/min and the highest onset crystallization temperature T_x = 800 K. The values of T_{max} and V_{max} increase, and T_x decreases in the sequence of inhibitors Nb, W, Mo, V, Cr.

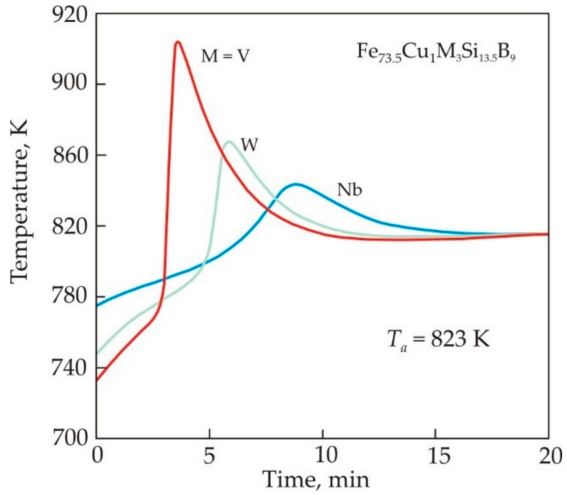

Figure 15. Change in time of the temperature of $Fe_{73.5}Cu_1M_3Si_{13.5}B_9$ cores, where M = Nb, W, V, during crystallization. Reproduced with permission from [77].

Figure 16 shows that the average grain size measured by a transmission electron microscope (TEM) grows in the sequence of inhibitors in Nb, W, Mo, V, Cr [77]. X-ray diffraction analysis confirms the relationship between the grain size and inhibitors for both the $Fe_{80}Si_{20}$ solid solution and the Fe_3Si phase.

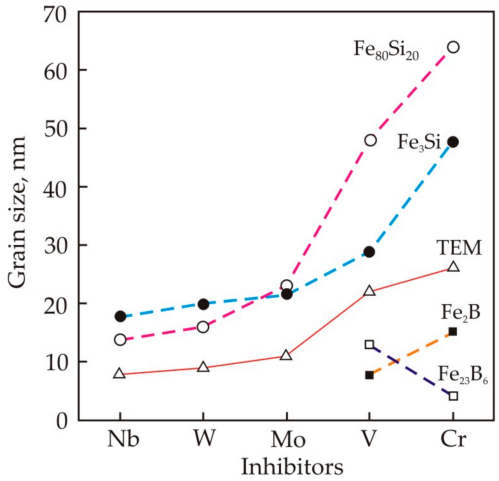

Figure 16. Average grain size from transmission electron microscopy (TEM) and average size of crystalline phases $Fe_{80}Si_{20}$, Fe_3Si, Fe_2B, and $Fe_{23}B_6$ from X-ray analysis in $Fe_{73.5}Cu_1M_3Si_{13.5}B_9$ alloys with inhibitors M = Nb, W, Mo, V, Cr. Reproduced with permission from [77].

The histograms of grain size distribution in $Fe_{73.5}Cu_1M_3Si_{13.5}B_9$ alloys with inhibitors Nb, W, Mo have several peaks, see Figure 17 [77]. In an alloy with Nb, the first peak falls at a size of 2 nm, but this peak is weakly expressed in an alloy with W and is absent in an alloy with Mo. In alloys with Nb, W, Mo, no grains larger than 30 nm were found. In alloys with V and Cr, the average grain size exceeds 20 nm, and the largest grains reach 80 nm. In these alloys, in addition to the $Fe_{80}Si_{20}$ solid solution and the Fe_3Si phase, Fe–B grains are also found, see Figure 16.

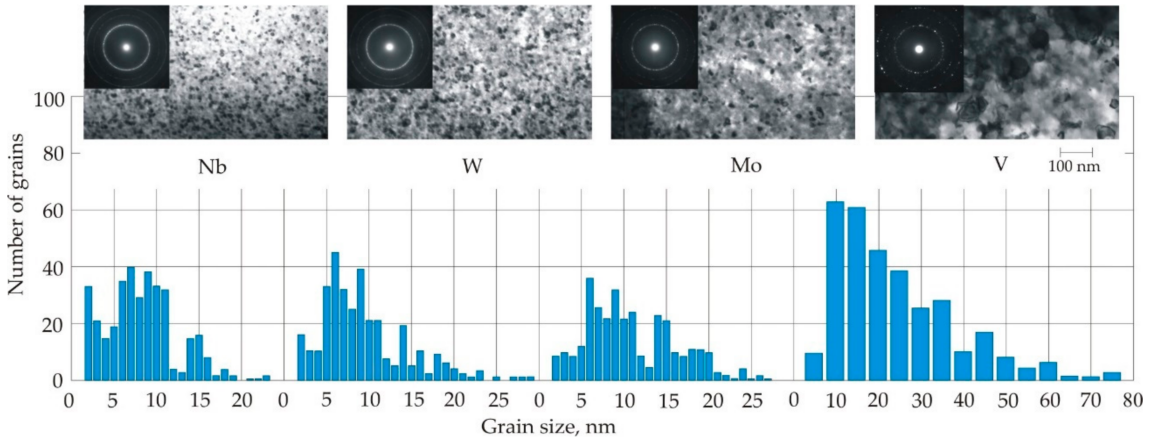

Figure 17. Histograms of grain size distribution and corresponding bright-field images with microdiffraction patterns in $Fe_{73.5}Cu_1M_3Si_{13.5}B_9$ alloys with inhibitors Nb, W, Mo, V. Reproduced with permission from [77].

Figure 18 shows the volume fraction of various crystalline phases in $Fe_{73.5}Cu_1M_3Si_{13.5}B_9$ alloys, where M = Nb, W, Mo, V, Cr, while the volume of all crystalline phases is taken as 100% [78]. It follows from the figure that the fraction of the $Fe_{80}Si_{20}$ solid solution decreases in the sequence Nb, W, Mo, V, Cr. The fraction of the Fe_3Si phase increases due Si diffusion in the $Fe_{80}Si_{20}$ solid solution. In alloys with V and Cr, the fraction of the Fe_3Si phase decreases due to the appearance of borides. Figure 18 also shows the dependence of the lattice parameter *a* for Fe_3Si phase after annealing at 823 K. According to [79], the lattice parameter of the pure Fe_3Si phase with the DO_3 structure is 0.5655 nm. In nanocrystalline alloys, the lattice parameter continuously increases in the sequence of Nb, W, Mo, V, Cr, and this indirectly indicates an improvement in the solubility of inhibitors.

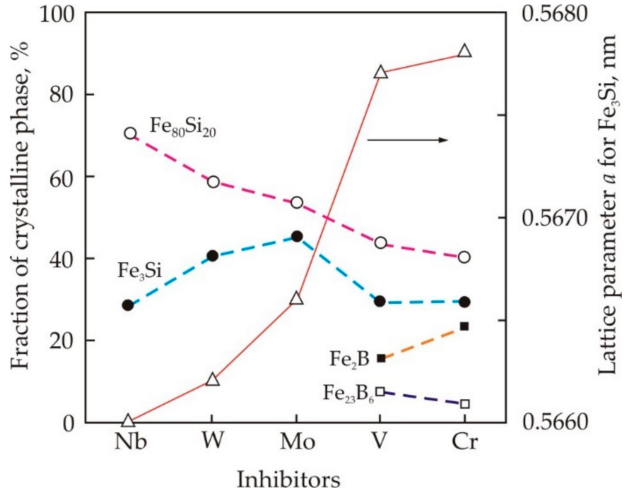

Figure 18. The volume fraction of various crystalline phases and the lattice parameter *a* for Fe_3Si phase in $Fe_{73.5}Cu_1M_3Si_{13.5}B_9$ alloys, where M = Nb, W, Mo, V, Cr. Reproduced with permission from [77].

The most effective inhibitors have large atomic sizes [80,81]. According to the Hume–Rothery rule [82], the solubility limit occurs when the size of the dissolved atoms is 15% larger than the solvent atoms. In accordance with this criterion, Nb are practically insoluble in αFe at 1000 K, and the solubility of other elements increases in the sequence Nb, W, Mo, V, Cr. With an increase in the solubility, the activation energy of diffusion naturally decreases.

Crystallization is accompanied by an increase in the volume of the crystalline phase due to the movement of grain boundaries. Impurity atoms interact with the moving

boundary. The boundary either attracts these atoms, and its speed of motion does not exceed the diffusion rate, or it breaks away from the atoms [83]. At a low migration rate, atoms with a lower diffusion mobility create a stronger inhibition, concentrating near the front of the moving boundary and not dissolving in the crystalline phase. Thus, the effect of inhibition of grain boundaries gradually weakens in the sequence Nb, W, Mo, V, Cr. The weakening of the inhibition is manifested in a decrease in the crystallization temperature T_x, as well as in an increase in the heating rate during crystallization V_{max} and the peak temperature T_{max}. A change in the migration rate of grain boundaries affects the depth of the crystallization process. Thus, the alloy with Nb has a structure that is typical for the initial stage of crystallization, namely, a large number of fine grains with a size of 2 nm, as well as a significant volume of the $Fe_{80}Si_{20}$ solid solution.

Table 3 shows the magnetic properties of nanocrystalline $Fe_{73.5}Cu_1M_3Si_{13.5}B_9$ alloys with different inhibitors after annealing at T_a = 823 K, 1 h [77]. It follows from the Table that all alloys, with the exception of alloys with V and Cr inhibitors, have high permeability and low coercive force. For the production of nanocrystalline soft magnetic materials, Mo, W and V are also used together with Nb [84–88]. It is known [89] that fine grain and high permeability are obtained after holding the core at a very high temperature, more than 870 K, but for a short time, i.e., the crystallization peak should be high and narrow. The height and width of the crystallization peak also depends on the dimensions of the core. Therefore, the size of the core can also affect the choice of the optimal chemical composition and crystallization regime.

Table 3. Magnetic properties of $Fe_{73.5}Cu_1M_3Si_{13.5}B_9$ alloys with different inhibitors after annealing at T_a = 823 K, 1 h. Reproduced with permission from [77].

Inhibitors	Initial Permeability $\mu_{0.08}$	Coercive Force H_c, $A \cdot m^{-1}$	Core Losses $P_{0.2/20}$, $W \cdot kg^{-1}$	Disaccommodation D_{90}
Nb	180,000	0.6	7.0	0.055
W	130,000	0.9	4.5	0.30
Mo	80,000	0.8	5.0	0.30
V	1400	45	-	-
Cr	100	550	-	-
$Mo_{0.5}Nb_{0.5}$	140,000	0.6	5.5	0.15
$Mo_{0.5}W_{0.5}$	110,000	0.9	4.0	0.35
$Mo_{0.5}W_{0.25}Nb_{0.25}$	150,000	0.5	4.0	0.15

Table 3 also shows that the drop in the initial permeability or disaccommodation 90 min after heat treatment is much lower in an alloy with Nb than in alloys containing W and Mo. The addition of Nb also reduces disaccomodation in alloys with a combined inhibitor system. The drop in permeability in a nanocrystalline alloy can be associated with the redistribution of vacancies in ferromagnetic nanocrystals containing impurity atoms [90] (pp. 537–551), [91]. Atoms of inhibitory elements occupy vacant positions in the substitutional solid solution, and large atoms contribute to a more intense formation of vacancies. Vacancies in nanocrystals can also pass from the amorphous matrix [92]. After demagnetization, which is accompanied by the motion of domain walls, vacancies in nanocrystals tend to occupy new stable states corresponding to new positions of domain walls. Redistributing, vacancies stabilize new positions of domain walls and cause a decrease in permeability. In an alloy with Nb, only a small number of inhibitor atoms are dissolved in α-FeSi and, accordingly, a smaller number of vacancies are formed.

Vacancies are concentrated near inhibitory atoms, promoting the formation of vacancy clusters, which can later grow into voids [39]. This process is most intense at elevated temperatures and can lead to aging. Domain walls are pinned at stable vacancy clusters, promoting an increase in the coercive force and a decrease permeability [90] (pp. 480–491). On the other hand, W atoms at a low concentration of 1–2 at. % decrease the lifetime and

stability of vacancy clusters [39]. This feature has a positive effect on the thermal stability of the nanocrystalline alloy with W [93].

The vacancy mechanism can be the reason for the decrease in core losses during aging of the nanocrystalline alloy, see Figure 19. In an alternating magnetic field, vacancy clusters can contribute to the domain refinement and a decrease in eddy current losses. At a high frequency, eddy current losses in a metallic magnetic material predominate, for example, their fraction at a frequency of 20 kHz in a nanocrystalline material with a thickness of 20 μm exceeds 80% [94]. A decrease in core losses at the initial stage of annealing was previously found in amorphous magnetic alloys [95,96]. It should be noted that immediately after heat treatment, nanocrystalline alloys containing W have the lowest core losses, see Figure 19 and Table 3.

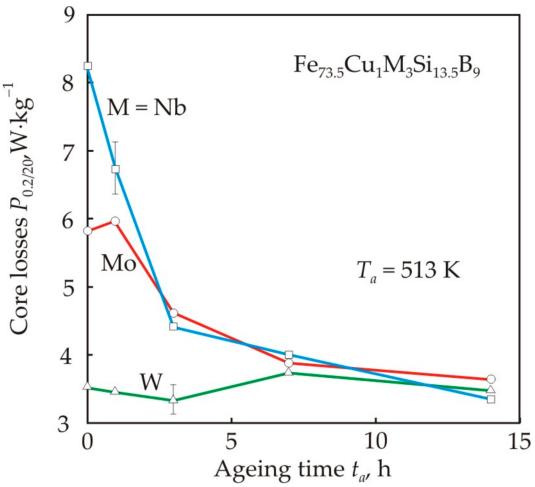

Figure 19. Dependences of the core losses $P_{0.2/20}$ (B_m = 0.2 T, f = 20 kHz) in $Fe_{73.5}Cu_1M_3Si_{13.5}B_9$ alloys, where M = Nb, W, Mo, on the aging time t_a at a temperature of T_a = 513 K. Reproduced with permission from [93].

5. Solute Elements in α-Fe

In the $Fe_{73.5}Cu_1Nb_3Si_{13.5}B_9$ alloy, Si is the soluble element in α-Fe. The Si content in nanocrystals plays a significant role in the formation of magnetic properties. In the Fe–Si binary alloy, an increase in the Si content to 11 at. % leads to a decrease in the crystallographic anisotropy constant K_1, and the saturation magnetostriction λs approaches zero [97]. In α-$Fe_{80}Si_{20}$ crystals, the magnetostriction takes on a negative value of -6×10^{-6}, and in the Finemet alloy the residual amorphous phase has a positive magnetostriction of about $+20 \times 10^{-6}$. Thus, to obtain a nanocrystalline alloy with a magnetostriction close to zero, a sufficiently large volume of the crystalline phase is required, which would compensate for the positive magnetostriction of the amorphous phase [15]. Taking into account that the volume fraction of the crystalline phase is about 0.7, the silicon content in a nanocrystalline alloy with zero magnetostriction should be about 16 at. %. It follows from Figure 20 that with an increase in the Si content in the $Fe_{73.5}Cu_1Nb_{31.5}Mo_{1.5}Si_bB_{22.5-b}$ nanocrystalline alloy, the magnetostriction approaches zero, and the permeability decreases [85] (p. 194).

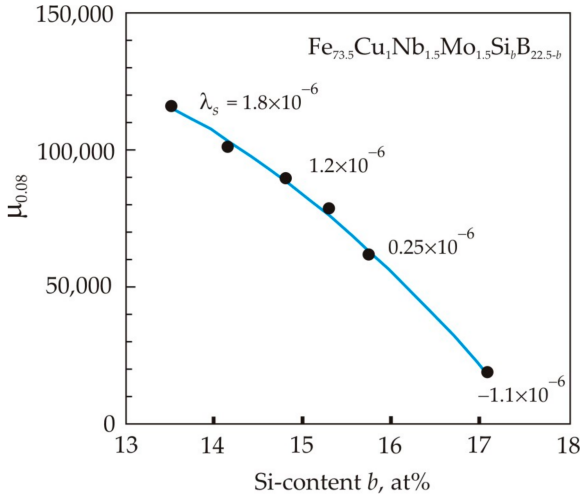

Figure 20. Dependence of the permeability $\mu_{0.08}$ on the Si content in the $Fe_{73.5}Cu_1Nb_{31.5}Mo_{1.5}Si_bB_{22.5-b}$ alloy. The numbers at the dots indicate the saturation magnetostriction λ_s of the corresponding alloys. Adapted from [85] (p. 194).

Magnetic-field-induced anisotropy is of a diffusion nature and is associated with directional ordering of Si-atom pairs [90] (pp. 299–309). Diffusion ordering occurs most intensely at high temperatures, but below the Curie point. Typical values of the annealing temperature of 813 K, Curie points of the crystalline phase at 873 K, and of the amorphous matrix at 573 K confirm that Fe–Si grains are the source of magnetic-field-induced anisotropy in the Finemet alloy [98]. During heat treatment, pairs of Si–Si atoms are oriented predominantly along the axis marked by an external magnetic field, and after cooling, this short-range order is retained with the formation of a stripe domain structure with 180° Bloch walls [99]. After annealing in a longitudinal magnetic field, the core has a square hysteresis loop (L) with high remanence ratio, and in a transverse field it has the flat shaped loop (T) with low remanence ratio, see Figure 21 [100]. After annealing without a magnetic field, pairs of Si–Si atoms are oriented in accordance with the local magnetic field, which is randomly oriented. This random ordering leads to local magnetic inhomogeneity and an increase in the coercive force, see loop O in Figure 21. The remanence ratio of round hysteresis loop is around 50%, typical for randomly oriented uniaxial anisotropy.

In the Fe–Si binary alloy, the induced magnetic anisotropy constant K_u takes the highest value at Si = 8–10 at. % [101,102], and the constant decreases with an increase in the Si content. The decrease in K_u with increasing Si content is associated with the formation of a Fe_3Si superlattice. The phase field of DO_3-type $Fe_{1-x}Si_x$ alloys extends over the composition range $0.15 < x < 0.25$ [103]. When $x = 0.25$, all lattice sites for the Fe and Si atoms will be occupied and therefore there is no freedom for an orientational ordering. The magnetic-field-induced anisotropy in Fe–Si nanocrystals of the Finemet alloy fully corresponds to the theory for the Fe–Si alloy, if we take into account the volume fraction of the crystalline phase [15,98]. With an increase in the external magnetic field, the ordering improves and the magnetic anisotropy constant increases [104].

Stress annealing of the $Fe_{73.5}Cu_1Nb_3Si_{13.5}B_9$ alloy leads to the formation of an in-plane magnetic anisotropy with easy axis perpendicular to the stress axis, which in the ribbon plane can be considered as uniaxial anisotropy with $K_u < 0$ [105]. The in-plane stress-induced anisotropy confirms the transverse domain structure with zigzag domain walls [106]. Figure 22 shows the hysteresis loops of the $Fe_{73.5}Cu_1Nb_3Si_{13.5}B_9$ nanocrystalline alloy after annealing at 803 K for 1h under the action of tensile stresses [105]. It can be seen that, with increasing stress, the slope of flat loops increases and this indicates a decrease in permeability.

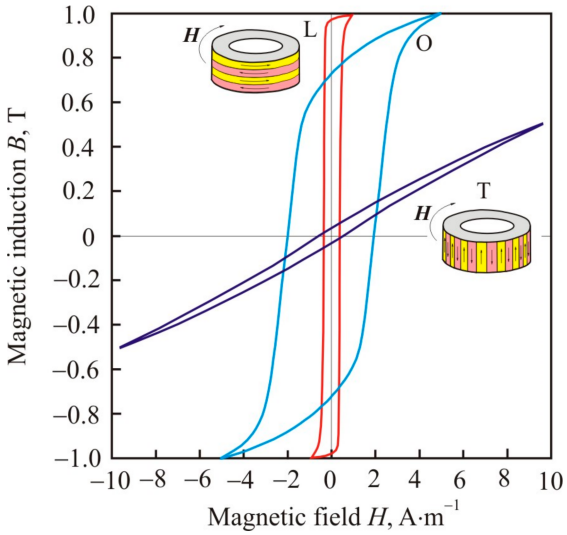

Figure 21. Magnetic hysteresis loops in the cores of the nanocrystalline $Fe_{67.5}Co_5Cu_1Nb_2Mo_{1.5}Si_{14}B_9$ alloy after heat treatment in a longitudinal (L) and transverse (T) magnetic field, as well as without a magnetic field (O). A stripe domain structure is shown schematically on the side faces of the L and T cores. Curved arrows show the direction of the external magnetic field during magnetization. Reproduced with permission from [100].

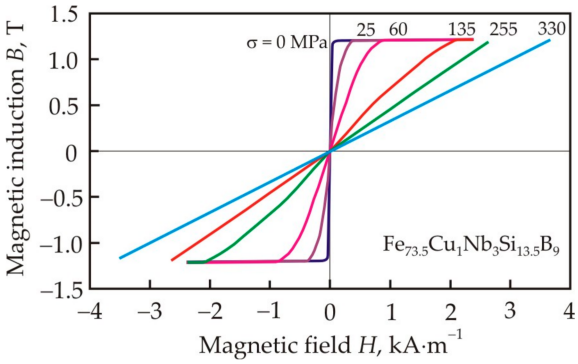

Figure 22. Magnetic hysteresis loops of the nanocrystalline $Fe_{73.5}Cu_1Nb_3Si_{13.5}B_9$ alloy after heat treatment under tension. The numbers next to the curves show tensile stress σ during nanocrystallization. Adapted from [105].

It was found in [107] that at a Si content of about 11 at. % in the $Fe_{87-x}Cu_1Nb_3Si_xB_9$ alloy, the type of stress-induced magnetic anisotropy changes. At a high Si content, transverse anisotropy with a flat loop is induced, and at a low Si content, longitudinal anisotropy with a square loop is induced. Nanocrystallization occurs under tension; therefore, after cooling and removal of the load, the crystal lattice of nanograins remains deformed and deformation is due to the internal stress. The interplanar spacing increases along the direction of the tensile stress, and decreases in the transverse direction. Direct evidence for permanent deformation in a nanocrystalline alloy was obtained in [108]. Internal stress will orient the magnetization in a direction that depends on the sign of magnetostriction. Since Fe–Si nanocrystals with a low Si content have positive magnetostriction, then in the $Fe_{87-x}Cu_1Nb_3Si_xB_9$ alloy, longitudinal magnetic anisotropy will form with the direction of magnetization along the tension axis. At a high Si content, the magnetostriction of nanocrystals is negative and transverse magnetic anisotropy with magnetization across the tension axis will form. Stress-induced anisotropy is associated with the magnetostriction

of the crystalline phase and internal stresses and does not depend on the presence of free pairs of Si–Si atoms, as in magnetic-field-induced anisotropy.

The introduction of Ni and Co soluble in α-Fe into a nanocrystalline alloy leads to an increase in the magnetic anisotropy constant K_u induced in a magnetic field [109]. Figure 23 shows the dependence of the magnetic anisotropy constant K_u on the Ni content in the $Fe_{72.5-x}Ni_xCu_{1.1}Nb_{1.9}Mo_{1.5}Si_{14.3}B_{8.7}$ alloy [110]. Linearity of the curve up to a Ni content of 7 at. % indicates that all newly dissolved Ni atoms contribute to the uniaxial induced anisotropy, participating in pair ordering. The weaker growth of K_u can be associated with a decrease in free pairs of atoms capable of rearranging in a magnetic field. It also follows from Figure 23 that the experimental constant determined from the magnetization work agrees well with the constant determined from the initial permeability μ_i in the model of magnetization rotation:

$$K_u = \frac{B_s^2}{2\mu_0\mu_i}. \quad (17)$$

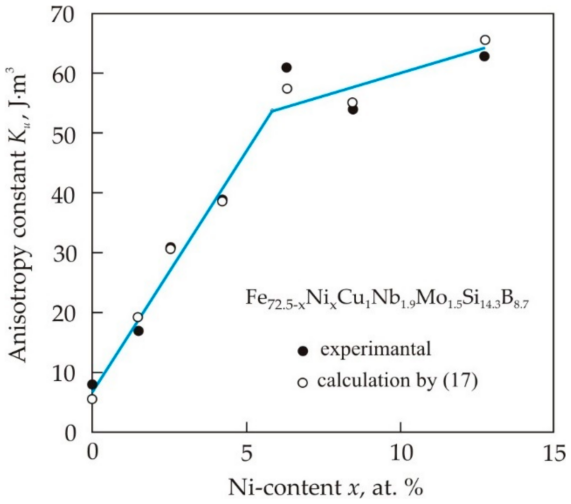

Figure 23. Dependence of the magnetic anisotropy constant K_u on the Ni content in the $Fe_{72.5-x}Ni_xCu_{1.1}Nb_{1.9}Mo_{1.5}Si_{14.3}B_{8.7}$ alloy calculated from the magnetization work and from the initial permeability μ_i by formula (17). Reproduced with permission from [110].

Figure 24 shows the dependences of temperature T and initial permeability μ_i at a frequency of 1 kHz on time t during crystallization of $Fe_{72.5-x}Ni_xCu_1Nb_2Mo_{1.5}Si_{14}B_9$ alloys with x = 0 and 8.5 at. % in a furnace with a fixed temperature of 823 K [111]. Nickel atoms in α-Fe have a low diffusion mobility and their solubility at 700 K does not exceed 5 at. % [112]. The smoothing of the crystallization peak in an alloy with Ni is similar to the effect of inhibitors, see Figure 15. The low diffusion mobility and limited solubility of Ni suggest that insoluble Ni atoms also have an inhibitory effect on crystal growth. The increased Ni content inhibits the formation of the crystalline phase, and the volume fraction of the amorphous phase increases [111]. X-ray analysis shows [111,113] that Ni in the crystalline phase is concentrated mainly in the Fe_3Si superlattice, partially replacing Fe atoms. Prolonged annealing of the alloy with Ni is accompanied by a strong increase in the coercive force [114], which can be associated with the formation of the tetragonal phase $Fe_3NiSi_{1.5}$ during the slow diffusion of Ni atoms [113].

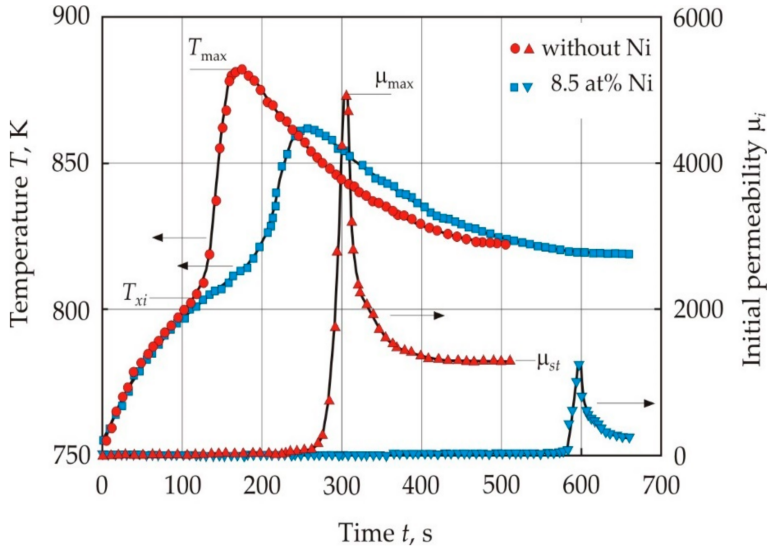

Figure 24. Time dependences of core temperature T and initial permeability μ_i in the crystallization process of $Fe_{72.5-x}Ni_xCu_1Nb_2Mo_{1.5}Si_{14}B_9$ alloys without Ni and with a Ni content of 8.5 at% at furnace temperature 823 K. Reproduced with permission from [111].

Figure 24 also shows the time dependence of permeability, which was measured continuously together with the core temperature [111]. As the Ni content increases, the temperature for the peak permeability μ_{max} decreases. This indicates an increase in the Ni content in the crystalline phase, since Ni lowers the Curie point of Fe-based alloys.

Another soluble element in α-Fe is Al, which is used in non-oriented electrical steel and in the sendust alloy $Fe_{73}Si_{17}Al_{10}$ with high permeability and low crystallographic magnetic anisotropy constant [115]. Partial substitution of Fe with Al improves magnetic properties of the nanocrystalline $Fe_{73.5-x}Al_xCu_1Nb_3Si_{13.5}B_9$ alloy [116].

Silicon plays an important role in the creation of a high permeability nanocrystalline alloy. Despite the rather high saturation magnetization J_s = 1.25 T, the $Fe_{73.5}Cu_1Nb_3Si_{13.5}B_9$ alloy cannot compete with the grain-oriented electrical steel, which has J_s = 2.03 T and is used at an industrial frequency of 50–60 Hz in power transformers. The low saturation magnetization in the Finemet is associated with the high Si content in the nanocrystals. To increase J_s, it is necessary to exclude as much as possible soluble nonmagnetic atoms in the crystal grain. In addition, a nanocrystalline material for industrial frequency should have a coercive force H_c of no more than 6 A·m^{-1}, this value corresponds to a typical coercive force for a grain-oriented electrical steel. Nanocrystalline soft magnetic materials have their advantages over electrical steel. Approximately two times higher electrical resistance and an order of magnitude less thickness give a significant reduction in eddy current losses.

At the stage of the preceding crystallization of a nanocrystalline alloy with an increased Fe content, the homogeneous amorphous matrix is separated into regions with different chemical compositions [117]. Crystallization of such regions leads to the formation of crystallites, which differ in size and magnetic anisotropy constants. In an alloy with a low Si content, the crystallization temperature decreases and the grain size increases, and this is associated with a weakening of the growth inhibition of Si-depleted grains. In nanocrystalline alloys with high saturation magnetization, Si is not used or is used as a small additive. To inhibit grain growth, Zr and B [118], P and B [119,120] or B alone [121,122] are used. To obtain finer grain an increase of heating rate is used during annealing [89,122,123]. Rapid heating at elevated temperatures allows the number of Cu-clusters to almost double [124], and a grain is formed whose size is about 30% smaller than with slow heating. In α-Fe nanocrystals in the absence of silicon, it is also possible to obtain a large magnetic anisotropy constant after annealing in a magnetic field, and this is due to the anisotropic distribution of interstitial atoms B, Zr, and Nb [125].

Figure 25 shows the dependence of the saturation magnetization J_s on the mass content of non-magnetic elements in nanocrystalline soft magnetic alloys with a coercive force less than 6 A·m^{-1}. The $Fe_{87}B_{13}$ alloy was obtained at a high heating rate of 3 K·s^{-1} [123]. It follows from the Figure that the saturation magnetization of the nanocrystalline alloy decreases in proportion to the mass fraction of non-magnetic elements [122].

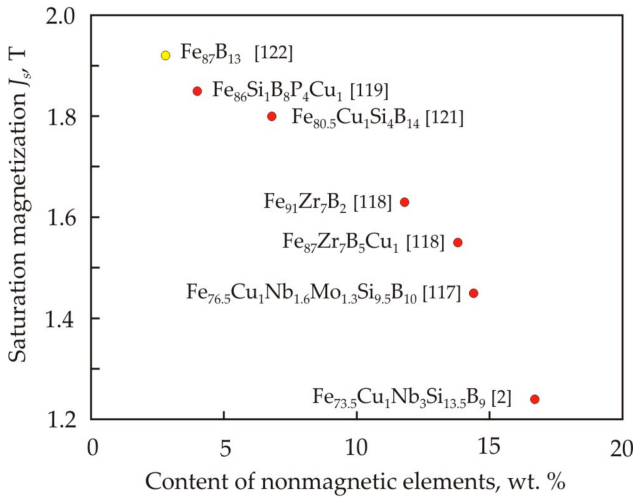

Figure 25. Dependence of saturation magnetization J_s on the mass content of non-magnetic elements in nanocrystalline soft magnetic alloys with a coercive force less than 6 A·m^{-1}. The $Fe_{87}B_{13}$ alloy was obtained at a heating rate of 3 K·s^{-1}.

6. Core Losses

Core losses determine the electromagnetic energy absorbed by a magnetic material. The work done by an electromagnetic field over a unit volume of material when the magnetic induction changes from B_1 to B_2 is equal to:

$$A = \int_{B_1}^{B_2} \mathbf{H}d\mathbf{B} = \mathbf{HB}\Big|_{B_1}^{B_2} - \int_{H_1}^{H_2} \mathbf{B}d\mathbf{H}, \tag{18}$$

and when changing along a full cycle,

$$A = -\oint \mathbf{B}d\mathbf{H} = \oint \mathbf{H}d\mathbf{B}. \tag{19}$$

The quantity of A is equal to the area of the magnetic hysteresis loop. A static hysteresis loop corresponds to an infinitely slow magnetization, and a dynamic loop is formed during a magnetization with a frequency f. The product of the area of the static hysteresis loop W_h, J·m^{-3}, by the frequency f is the hysteresis losses P_h, and the product of the area of the dynamic hysteresis loop by the frequency is the total losses P.

In essence, the magnetization is the rotation of the atomic magnetic moments, which is accompanied by the precession of magnetization and is described by the Landau–Lifshitz equation [90] (pp. 562–566). Friction leads to damping of precession and the approach of the magnetization vector to the direction of the external magnetic field. Magnetic relaxation is associated with the interaction of carriers of magnetic moments with each other (spin-spin relaxation) and their environment (spin-lattice relaxation). As a result of magnetic relaxation, the energy of motion of the magnetic moments transforms into heat, and the system tends to a state of thermodynamic equilibrium. Relaxation losses are the main source of high-frequency losses in non-metallic magnetic materials; however, in metallic materials against the background of eddy currents, they are in many case insignificant.

The nature of eddy current losses is evident from classical electrodynamics. However, in ferromagnetic materials, it is necessary to take into account the features caused by the magnetic domain structure. In a ferromagnet, a change in magnetic induction occurs only near a moving domain wall, and eddy currents are also concentrated here. Therefore, with an increase in the size of the domains, the inhomogeneity of the magnetization increases. The eddy current losses P_{ed}, W·kg^{-1}, in the model of flat domain walls are proportional to the domain width D [126] and under the condition $D > h$, h is the plate thickness, m, they are equal to:

$$P_{ed} \approx 1.628 \frac{D}{h} P_c, \tag{20}$$

where P_c is the classic eddy current losses for a uniform magnetic flux

$$P_c = \frac{\pi^2 B_m^2 h^2 f^2}{6\rho} \tag{21}$$

and B_m is the amplitude of sinusoidal magnetic induction, T, f is the frequency, Hz, ρ is the electrical resistivity, Ω·m. If the domain width is less than the ribbon thickness, then the magnetic flux in the material is more uniform, and P_{ed} approach the classical eddy current losses P_c.

The influence of eddy currents and magnetization relaxation illustrates the frequency dependence of the permeability in a metal nanocrystalline alloy and ferrite, see Figure 26 [19] (p. 69).

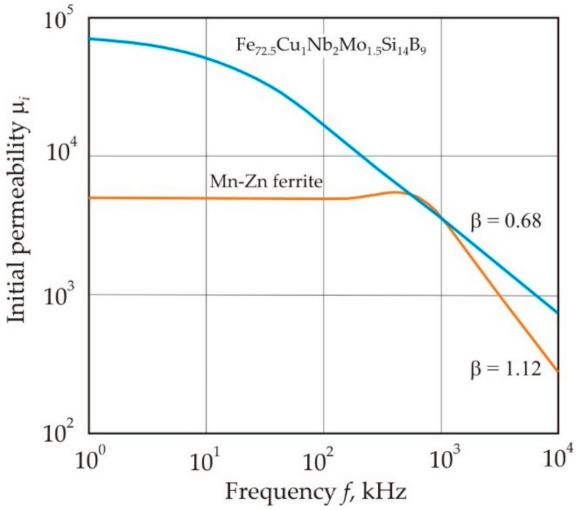

Figure 26. Frequency dependence of the initial permeability μ_i in nanocrystalline $Fe_{72.5}Cu_1Nb_2Mo_{1.5}Si_{14}B_9$ alloy and Mn–Zn ferrite. Reproduced with permission from [19] (p. 69).

In the high-frequency region, the exponent β of the power function:

$$\mu_i \propto f^{-\beta} \tag{22}$$

equal to 0.68 and 1.12 for the metal $Fe_{72.5}Cu_1Nb_2Mo_{1.5}Si_{14}B_9$ alloy and Mn-Zn ferrite, respectively, i.e., in ferrite, the decrease in μ_i with frequency is steeper. These exponents are close to 0.5 for the penetration depth of the magnetic field:

$$\delta_H = \sqrt{\frac{\rho}{\pi \mu \mu_0 f}} \tag{23}$$

which decreases under the influence of eddy currents, and 1.0 for the frequency dependence of the permeability caused by the magnetization relaxation,

$$\mu = \mu_i \frac{\omega_0^2}{2\lambda\omega} \tag{24}$$

where λ and ω_0 are the damping coefficient and natural frequency of the domain wall oscillation [85] (pp. 123–127).

Hysteresis is associated with the existence of stable and metastable states in the material and with irreversible transitions between these states. In soft magnetic materials, irreversible displacement of domain walls is the main cause of hysteresis. During magnetization, the domain wall or its individual sections jump into new equilibrium states. Such a jump is accompanied by a local change in the magnetic induction and the corresponding local eddy currents. The time interval between jumps depends on the density of defects and the velocity of motion of domain walls. If the duration of a jump is less than the time interval between two successive jumps, then the overlap of eddy currents from adjacent jumps does not occur. Domain wall jumps can occur simultaneously and not overlap due to their remoteness in space. In this case, the magnetic losses per cycle are equal to the sum of the eddy current losses arising from individual jumps. These local eddy current losses are frequency independent and are essentially hysteresis losses.

Eddy currents caused by jumps begin to overlap in time and space with an increase in the velocity of domain wall movement, i.e., with increasing frequency and induction, and this leads to the dependence of magnetic losses on frequency.

Figure 27 shows the dependences of the hysteresis losses W_h on the maximum induction B_{max} after heat treatment in a longitudinal (L) and transverse (T) magnetic field, as well as without a magnetic field (O), for cores made of a nanocrystalline $Fe_{67.5}Co_5Cu_1Nb_2Mo_{1.5}Si_{14}B_9$ alloy [100]. On the curves in the logarithmic scale, one can select linear sections that correspond to a constant exponent s for the approximating power function:

$$W_h = rB_{max}^s \tag{25}$$

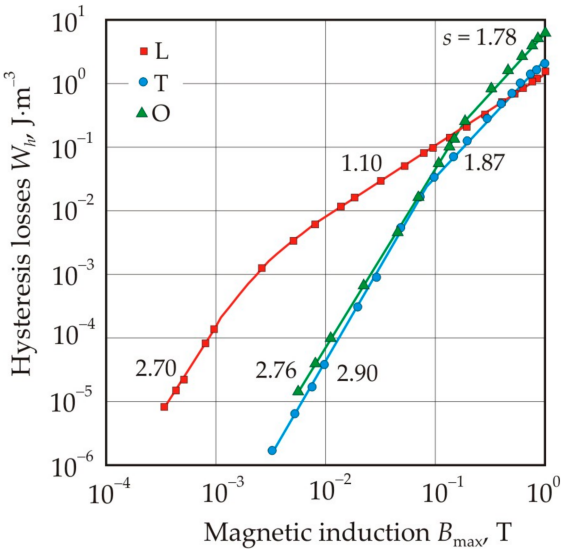

Figure 27. Dependences of hysteresis losses W_h on the maximum induction B_{max} after heat treatment in a longitudinal (L) and transverse (T) magnetic field, as well as without a magnetic field (O), for cores made of nanocrystalline $Fe_{67.5}Co_5Cu_1Nb_2Mo_{1.5}Si_{14}B_9$ alloy. The numbers on the curves represent the exponent s for the power function (25). Reproduced with permission from [100].

The power function is scale invariant. This means that all power functions with the same exponent s are equivalent to each other and differ only in scale, i.e., in the coefficient

r. Thus, the constant s in a certain interval of the independent variable, in our case B_{max}, can be associated with the invariability of the process described by this power function. Conversely, a change in the exponent s should indicate a qualitative change in this process.

As can be seen from Figure 27, in a weak magnetic field, the core L with longitudinal uniaxial anisotropy has the greatest hysteresis losses [100]. In this core, at B_{max} = 0.0025 T, the exponent s changes the value 2.70, which is close to exponent 3 in Rayleigh's law, by 1.10. At the same magnetic induction, the hysteresis loop changes the lens-like shape with a low remanence ratio, which is typical for the Rayleigh region, to a square one, see Figure 28.

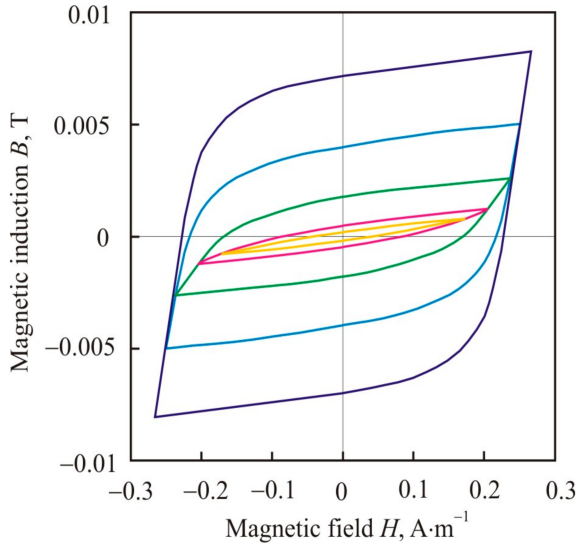

Figure 28. Minor magnetic hysteresis loops in the L core with longitudinal induced anisotropy for the nanocrystalline $Fe_{67.5}Co_5Cu_1Nb_2Mo_{1.5}Si_{14}B_9$ alloy in a weak magnetic field. Reproduced with permission from [100].

The change in the shape of the hysteresis loop can be interpreted as follows. The loop has a square shape if most of the domain walls almost simultaneously overcome the maximum local potential barriers. In the Rayleigh region, a reversible displacement of domain walls predominates, and this displacement should be small and not exceed the characteristic length of the local magnetic inhomogeneity of the material. In a nanocrystalline alloy, the scale of the magnetic inhomogeneity is related to the correlation length L_{ex}, i.e., to the size of ferromagnetic clusters. The increment in magnetic induction ΔB with displacement of flat domain walls by a distance L_{ex} is:

$$\Delta B = \frac{2J_s}{D} L_{ex} \tag{26}$$

where D is the domain width, J_s is the saturation magnetization. For the assessment we use the following values J_s = 1.2 T and $D = 10^{-3}$ m [127], correlation length $L_{ex} = 10^{-6}$ m. These values give an increment in magnetic induction ΔB = 0.0024 T, which is close to 0.0025 T obtained from Figure 27 for the Rayleigh region in core L.

If there is a periodic change in the local magnetic energy density ΔE in a ferromagnetic material, then the coercive force associated with a delay in the displacement of domain walls at these inhomogeneities can be expressed in the form [90] (pp. 487–491):

$$H_c \approx \frac{\Delta E}{\mu_0 M_s} \frac{\delta}{l} \tag{27}$$

where δ is the width of the domain wall, l is the characteristic length of the magnetic inhomogeneity. In a nanocrystalline alloy, $\Delta E = \langle K \rangle$ and $l \approx L_{ex}$. The largest coercive force

is obtained under the condition $l = \delta$. For a nanocrystalline alloy, $\delta \approx L_{ex}$ and the coercive force associated with the random distribution of the easy axes in ferromagnetic clusters is:

$$H_c \approx \frac{\langle K \rangle}{\mu_0 M_s} \tag{28}$$

After annealing in a magnetic field, the easy magnetization axes in ferromagnetic clusters are concentrated in a certain solid angle, which narrows with an increase in the induced magnetic anisotropy constant K_u. In this case, the differences between the orientations of the easy magnetization axes of neighboring clusters are smoothed out. Such smoothing is equivalent to a decrease in the inhomogeneity ΔE, and should lead to a decrease in the coercive force. This mechanism explains the decrease in the coercive force in the L core after annealing in a longitudinal magnetic field compared to the O core, which was annealed without a magnetic field.

For core T, the dependence of hysteresis losses on magnetic induction in a weak magnetic field has an exponent $s = 2.90$, which corresponds to Rayleigh's law, see Figure 27. The exponent does not change up to a magnetic induction of 0.08 T. Thus, the Rayleigh region in the core T is an order of magnitude larger compared with the core L. The value $B_{\max} = 0.08$ T separates the regions of uniform reversible rotation of magnetization, typical for a weak magnetic field, and inhomogeneous irreversible rotation.

The mechanism of irreversible magnetization rotation can be as follows [100]. In a nanocrystalline material, the easy magnetization axes of ferromagnetic clusters are randomly distributed. In a material with induced magnetic anisotropy K_u, the easy magnetization axes of clusters are concentrated near the direction of the magnetic field during heat treatment. In Figure 29, double arrows show the axes of easy magnetization of the clusters [100]. The $\boldsymbol{M}_s$ vector denotes the direction of magnetization in the magnetic domain. Without an external magnetic field, the magnetization in neighboring clusters is directed towards the number 1 in Figure 29. In an external magnetic field $\boldsymbol{H}$ directed at an angle of 90° to the easy magnetization axis K_u, the magnetization of the clusters rotates to the direction $\boldsymbol{H}$. In the left cluster, the rotation from direction 1 will lead to an increase in the angle between the cluster magnetization and its easy magnetization axis, i.e., to an increase in the magnetic anisotropy energy. Therefore, at some moment, direction 1 will become unstable and an irreversible magnetization rotation by 180° in the direction closest to the direction of the external magnetic field will occur. In the right cluster in Figure 29, the magnetization will smoothly rotate towards the direction of the magnetic field. Thus, many ferromagnetic clusters can experience an irreversible magnetization rotation towards the direction of the external magnetic field. The mechanism of irreversible magnetization rotation in a nanocrystalline material is similar to the irreversible rotation that occurs in a particle with uniaxial magnetic anisotropy [90] (pp. 491–498).

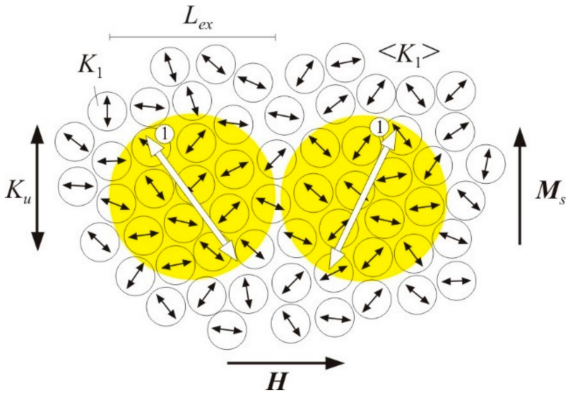

Figure 29. Schematic representation of the irreversible magnetization rotation in a nanocrystalline material with induced transverse magnetic anisotropy. Reproduced with permission from [100].

Comparison of hysteresis losses for O and T cores in the Figure 27 shows that they practically do not differ up to B_{max} = 0.08 T. Further, the curves diverge due to a faster growth of hysteresis losses in the core O. This proves that the mechanisms of magnetic hysteresis in O and T cores in a weak magnetic field are the same or close, and the main role is assigned to reversible rotation of magnetization [128].

From the Rayleigh equations, one can find relations connecting the parameters of the hysteresis loop [129,130], in particular, the hysteresis losses can be calculated by the formulas:

$$W_h = \frac{8}{3} B_{max} H_c \quad (29)$$

$$W_h = \frac{8}{3} B_r H_{max} \quad (30)$$

$$W_h = \frac{8}{3} \sqrt{B_r B_{max} H_c H_{max}} \quad (31)$$

In core O with a round hysteresis loop, the difference between the measured and calculated hysteresis losses for formulas (29)–(31) does not exceed 2% [100]. In L and T cores with induced magnetic anisotropy, the convergence is worse and it is in the range of 8–20% for cores with different types of anisotropy and for different formulas.

Figure 30 shows the dependences of the core losses P on the amplitude of the magnetic induction B_m and the frequency f for the nanocrystalline $Fe_{72.5}Cu_1Nb_2Mo_{1.5}Si_1$ alloy [94]. It follows from the Figure that the $P(B_m)$ dependences on a logarithmic scale have two linear sections with different slopes, and at a frequency above 20 kHz, the curves degenerate into one straight line. The dashed line marks transition points that are close to B_m = 0.1 T. Each curve in the frequency dependence of core losses in Figure 30 also has two linear sections with transition points at a frequency of 3 kHz, at which the skin effect begins to appear in a 25 μm thick ribbon [94].

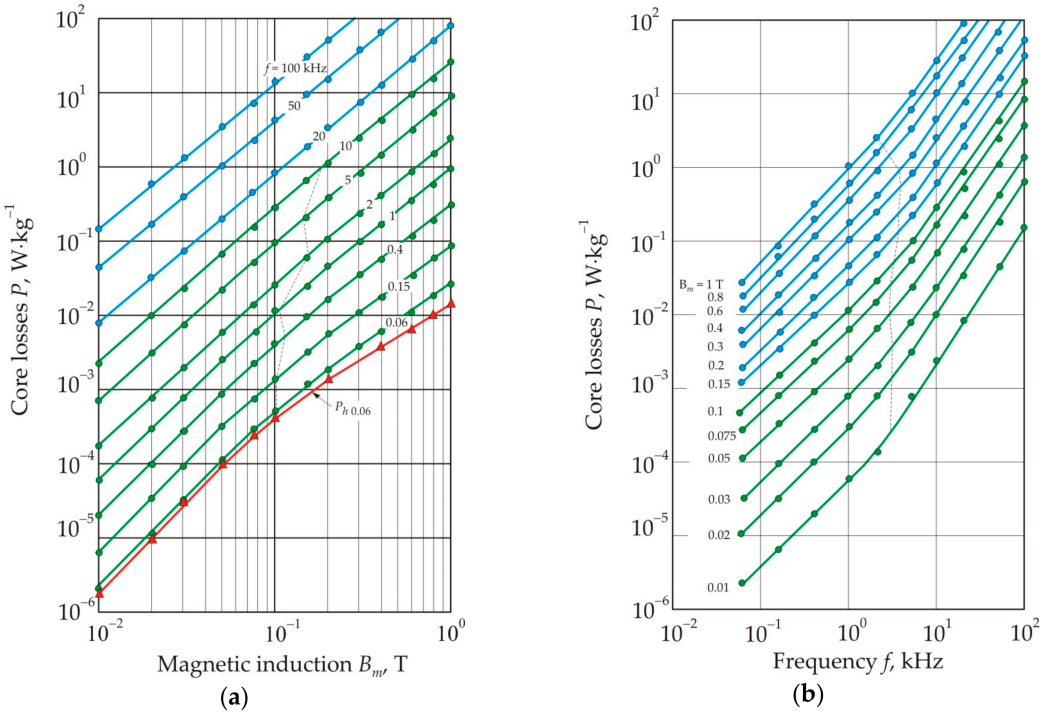

Figure 30. Dependences of core losses P on magnetic induction Bm at different frequency f (**a**) and dependences of core losses P on frequency f for different magnetic induction Bm in the Fe72.5Cu1Nb2Mo1.5Si14B9 alloy after heat treatment without a magnetic field. The numbers on the curves indicate the frequency f in kHz (**a**) and the magnetic induction Bm in T (**b**). Curve $Ph60$ corresponds to hysteresis losses at a frequency of 60 Hz. The dashed line marks the transition points that correspond to the change in the slope of the linear sections of the curves. Reproduced with permission from [94].

Figure 31 shows the dependences of the ratio of hysteresis losses to total magnetic losses P_h/P on magnetic induction B_m at different frequencies [94]. Hysteresis losses P_h, W·kg^{-1}, were determined from the ratio:

$$P_h = \frac{W_h}{\rho} f, \tag{32}$$

where ρ is the density. It follows from Figure 31 that hysteresis losses prevail in a weak magnetic field and at a low frequency, and here their fraction reaches 90%. In this region, the total loss curves are close to the hysteresis loss curves, see Figure 30a. Fraction of eddy current losses increases at high magnetic induction B_m, when the motion of domain walls becomes smooth, and in the high-frequency region.

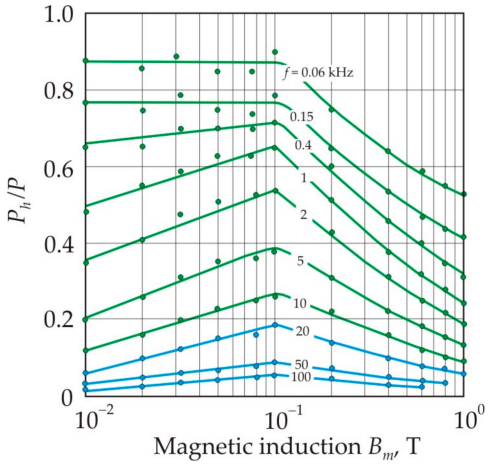

Figure 31. Ratio of hysteresis losses P_h to total magnetic losses P as a function of magnetic induction B_m in nanocrystalline alloy $Fe_{72.5}Cu_1Nb_2Mo_{1.5}Si_{14}B_9$ at different frequency f. Reproduced with permission from [94].

Figure 32 shows the frequency dependences of the exponent s for the approximating power function (25) in a weak (B_m = 0.01 T) and middle (B_m = 0.6 T) magnetic field. In a weak magnetic field, hysteresis losses predominate and the exponent is close to 3, which is characteristic of Rayleigh hysteresis loops. At high frequency, core losses are associated with eddy currents, and the exponent s approaches 2 in accordance with formulas (20) and (21). The exponent s = 1.6 corresponds to the approximate balance of hysteresis and eddy current losses [131].

By comparing the measured eddy current losses $P_{ed} = P - P_h$ with formula (20), one can calculate the number of domain walls involved in the magnetization. Calculations show that the number of domain walls increases with increasing frequency, see Figure 33 [85] (pp. 212–214). This fact follows from the principle of minimum entropy production, according to which the frequency dependence of the domain width D is a power function of frequency with exponent $s = -0.5$ [132] and accordingly, the exponent s = 0.5 for the number of domain walls.

It follows from Figure 33 that the number of domain walls is larger in a weak magnetic field at B_m = 0.01 T. An increase in the number of domain walls can be associated with the special role of ferromagnetic clusters in the absence of induced magnetic anisotropy [133]. The cluster structure of a nanocrystalline material is a magnetic inhomogeneity that promotes the domain refinement in an alternating magnetic field [134,135]. In the low-frequency region at B_m = 0.6 T, there is a smooth motion of domain walls, and the exponent s is closest to 0.5. At frequencies above 3 kHz, the skin effect begins to prevail, and the number of domain walls weakly depends on the frequency.

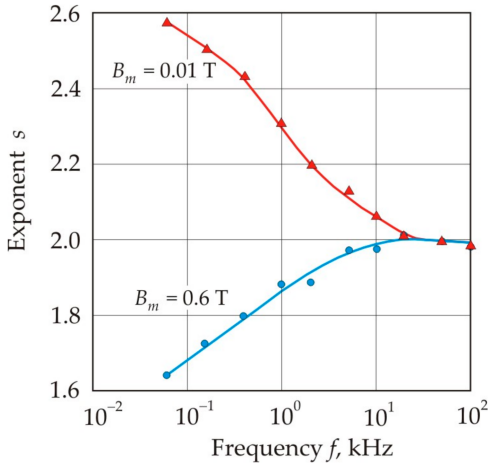

Figure 32. Frequency dependences of the exponent s for the approximating power function (25) in the nanocrystalline $Fe_{72.5}Cu_1Nb_2Mo_{1.5}Si_{14}B_9$ alloy at magnetic induction B_m = 0.01 and 0.6 T. Reproduced with permission from [94].

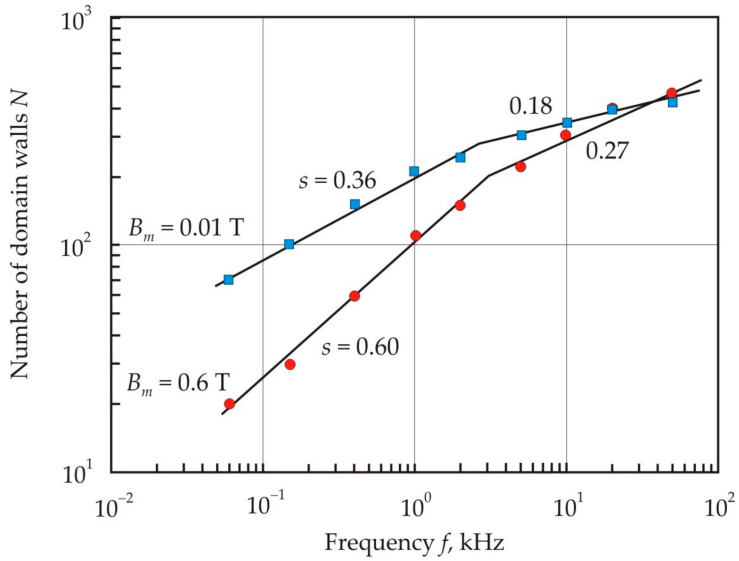

Figure 33. Frequency dependence of the calculated number of domain walls N for B_m = 0.01 and 0.6 T in a 10 mm wide ribbon made of nanocrystalline $Fe_{72.5}Cu_1Nb_2Mo_{1.5}Si_{14}B_9$ alloy. The numbers on the curves show the exponent s for the approximating power function. Adapted from [85] (pp. 212–214).

7. Applications

Figure 34 shows the relationship of the initial permeability μ_i with the coercive force H_c (a) and the saturation magnetization J_s (b) for soft magnetic materials [19] (pp. 117–121). The closed curves mark the areas corresponding to various materials of the same name, and the dots mark the most famous soft magnetic materials. It can be seen that a good correlation between μ_i and H_c takes place for a wide variety of soft magnetic materials, ferromagnetic and ferrimagnetic, crystalline, nanocrystalline, and amorphous.

Magnetic materials are used mainly in the temperature range from 220 to 380 K, and reference magnetic properties are given for the same temperature range. Soft magnetic materials with a Curie point near the upper boundary of this interval have the highest magnetic permeability [136], because the magnetic anisotropy constant is lower here. Near the Curie point, the saturation magnetization is also lower and, therefore, there is a tendency to a increase in permeability with decreasing saturation magnetization, see Figure 34b. In non-metallic ferrites, such a connection is absent.

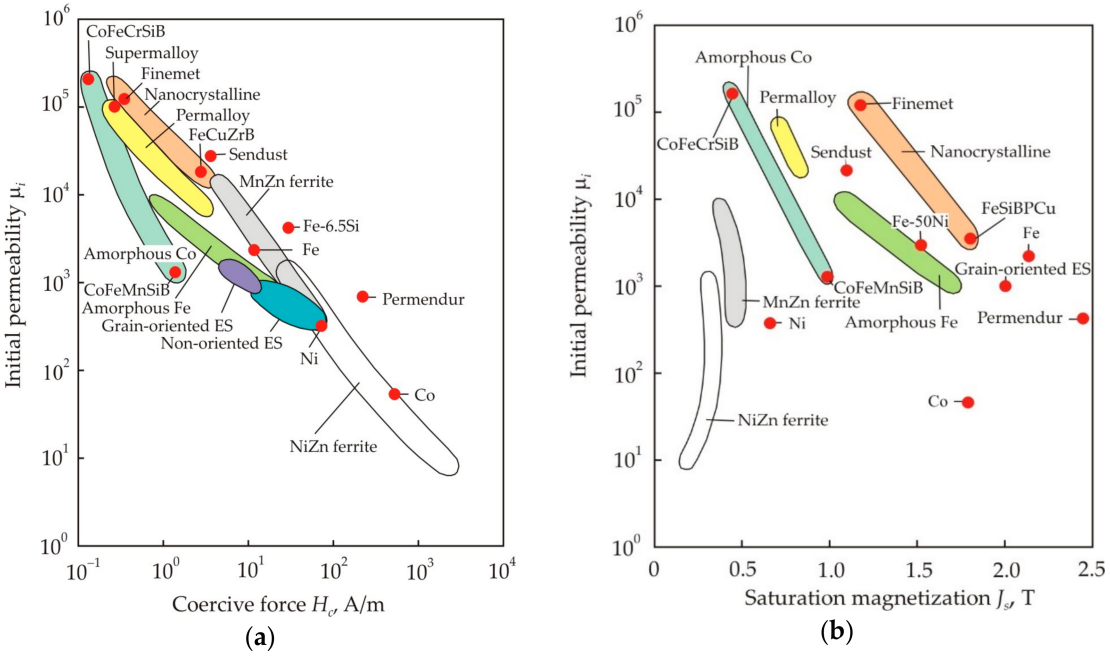

Figure 34. Relationship of initial permeability μ_i with coercive force H_c (**a**) and saturation magnetization J_s (**b**) for soft magnetic materials. Reproduced with permission from [19] (pp. 117–121).

Nanocrystalline soft magnetic materials of the Finemet type have high permeability, up to 100,000, which is achieved at a sufficiently high saturation magnetization, J_s = 1.25 T. A thin ribbon, 20 μm, together with a low coercive H_c, less than 1 A·m^{-1}, provide low core losses in a wide frequency range. Magnetic anisotropy, induced in a magnetic field or under stress, allows the formation of a linear hysteresis loop with a low remanence ratio and permeability from 100 to 100,000 or a round hysteresis loop with a high remanence ratio. Nanocrystalline soft magnetic materials are used for frequencies from 50 Hz, for example, for high-precision current transformers, and up to 10 MHz, for example, for attenuation of common-mode noises [137]. The use of nanocrystalline materials in traditional components and devices improves the electromagnetic properties of these products [19] (pp. 277–345), [138].

In power electronics, nanocrystalline materials are most commonly used for transformers and electrical reactors or chokes. Figure 35 shows the power of transformers P_t with a magnetic core, which has an outer diameter of 20 mm, an inner diameter of 32 mm and a height of 10 mm [139]. The core was made of grain-oriented electrical steel 0.08 mm thick, MnZn ferrite with permeability 2000, and nanocrystalline $Fe_{72.5}Cu_1Nb_2Mo_{1.5}Si_{14}B_9$ alloy. The calculation was carried out for a transformer overheating temperature of no more than 20 K, a current density in the windings of 3 × 10^6 A·m^{-2}, and a window fill factor for the wires of the primary and secondary windings of 0.2.

From Figure 35 it follows that up to almost 100 kHz, the power of a nanocrystalline alloy transformer is higher compared to other transformers. An exception is an electrical steel transformer with a frequency of less than 1 kHz. Higher power in such a transformer is provided by a higher saturation magnetization in electrical steel. The power of the nanocrystalline alloy transformer rises sharply to a frequency of about 7 kHz. Such an increase is associated with a continuous increase in the operating induction of the transformer to a limit value of 1.1 T. At an increased frequency, the operating induction has to be reduced in order to meet the overheating temperature requirement. In a ferrite transformer, the maximum operating induction is achieved already at a frequency of less than 1 kHz. In the frequency range from 1 to 10 kHz, nanocrystalline magnetic cores have a significant advantage over other soft magnetic materials.

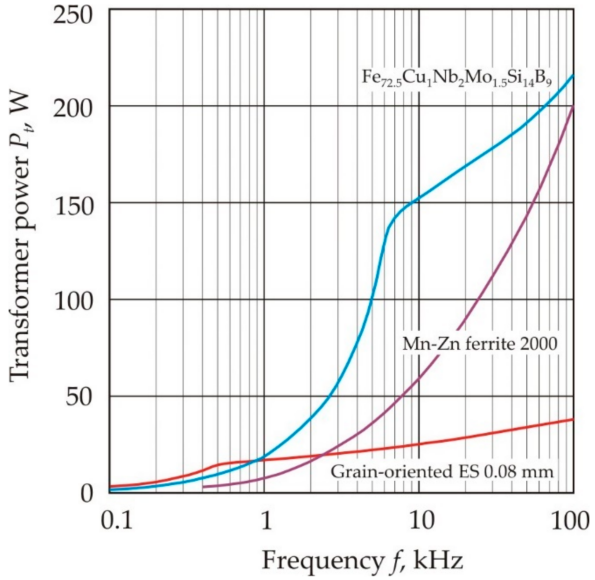

Figure 35. Power of transformers P_t as a function of frequency f for a magnetic core made of different soft magnetic materials, which has an outer diameter of 20 mm, an inner diameter of 32 mm and a height of 10 mm. Adapted from [139].

The shape of the magnetic cores greatly affects the distribution of the magnetic flux. Figure 36 shows the distribution of magnetic induction B in cores with a cross section of 60 × 125 mm, which are made of nanocrystalline $Fe_{72.5}Cu_1Nb_2Mo_{1.5}Si_{14}B_9$ alloy [19] (p. 96). The cores had different radius of curvature at the junction of the limb and yoke. The magnetic field was created by a winding of 15 turns on each limb, through which a current of 0.5 A flowed.

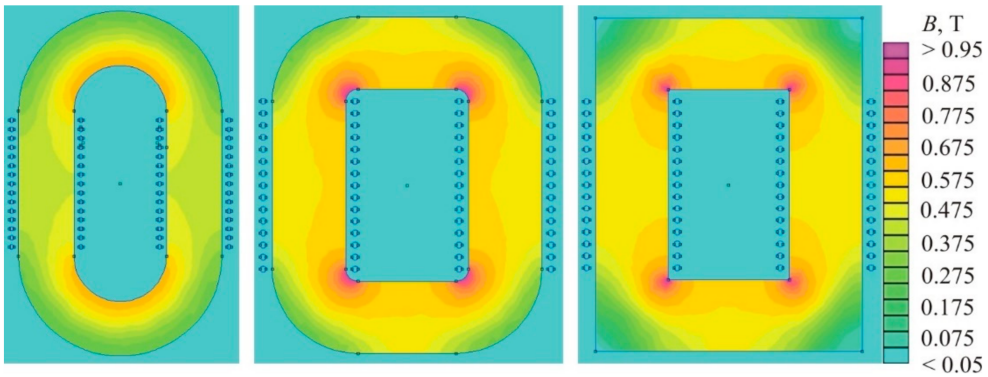

Figure 36. Distribution of magnetic induction B in cores made of nanocrystalline $Fe_{72.5}Cu_1Nb_2Mo_{1.5}Si_{14}B_9$ alloy and having different shapes. Reproduced with permission from [19] (p. 96).

Figure 36 shows that the magnetic induction is almost uniformly distributed in the straight limbs [140]. The inhomogeneity of the magnetic induction appears due to the curvature of the magnetic field lines at the junction of the limb and yoke. The inhomogeneity is higher with a smaller radius of curvature. The core with right angles has the greatest inhomogeneity. In the inner areas of the corner, the magnetic induction reaches 1.1 T, while the peripheral areas are almost not magnetized.

To store high magnetic energy, the core of an electric reactor (choke) must have a low permeability. In small reactors, cores of magnetodielectric materials are used, which are obtained by pressing magnetic particles isolated from each other. An alternative is the cut magnetic cores. Figure 37 compares the core losses at f = 20 kHz and B_m = 0.2 T in magne-

todielectrics and in cut cores made of nanocrystalline $Fe_{72.5}Cu_1Nb_2Mo_{1.5}Si_{14}B_9$ alloy [140]. Magnetodielectrics made of Mo-permalloy, sendust, and $Fe_{72.5}Cu_1Nb_2Mo_{1.5}Si_{14}B_9$ alloy have approximately the same level of core losses, but only for permeability below 140. High permeability cores are best made from nanocrystalline soft magnetic materials. A significant increase in losses in magnetodielectrics with a permeability above 140 is associated with a decrease in the dielectric properties of the insulation between the magnetic particles.

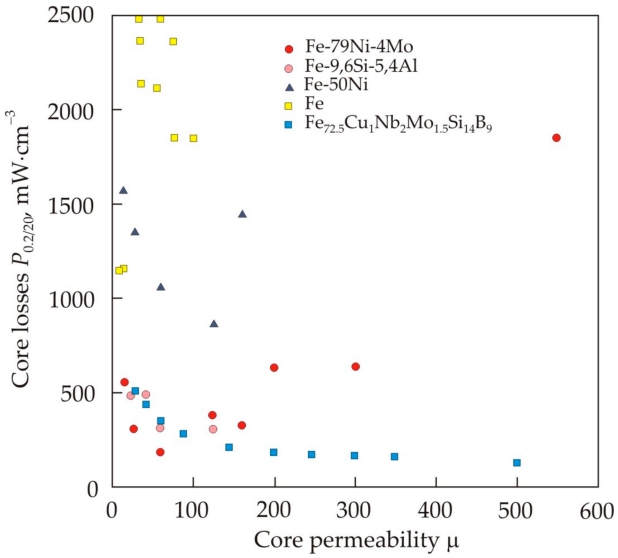

Figure 37. Core losses in magnetodielectric cores and cut cores made of nanocrystalline $Fe_{72.5}Cu_1Nb_2Mo_{1.5}Si_{14}B_9$ alloy. Adapted from [140].

8. Conclusions

The review analyzes the physical processes occurring at different stages of the production and application of nanocrystalline soft magnetic materials. The object of the study was Fe–Si–B alloys doped with various chemical elements, which have found wide practical application.

When a multicomponent melt is heated above a certain critical temperature, the melt viscosity at the cooling stage does not coincide with the viscosity at the heating stage, and the heating and cooling curves can form a hysteresis loop. The critical temperature is associated with the rearrangement of the melt structure, in particular, with the formation of a more uniform structure in the high-temperature region. An amorphous precursor from a homogeneous melt has a higher plasticity and enthalpy of crystallization, and after nanocrystallization, a material with a higher permeability is obtained.

The most effective inhibitor elements have a large atomic size, they are practically insoluble in α-Fe and form a smoothed peak of heat release during crystallization. On the other hand, the finest nanograins and the highest permeability are obtained when the heat release has a narrow high-temperature peak. The role of soluble elements in the formation of magnetic anisotropy induced by the magnetic field and stress is shown.

The cluster magnetic structure of nanocrystalline alloys is manifested in magnetic inhomogeneity. The influence of magnetic inhomogeneity on the shape of the magnetic hysteresis loop and on core losses is shown, and the mechanism of irreversible magnetization rotation is considered.

Nanocrystalline soft magnetic materials based on iron have a whole set of magnetic properties, which made it possible to expand their application in a short time. The nanocrystalline alloys have high saturation magnetization and permeability, low coercive force, magnetostriction and core losses, as well as the ability to change the shape of the hysteresis loop due to magnetic-field-induced or stress-induced anisotropy. Further research in the field of nanocrystalline soft magnetic materials is aimed at developing new efficient and economical nanocrystalline materials, including those with high saturation magnetization

for an industrial frequency. An important task remains the development of new magnetic components and electromagnetic devices based on already available nanocrystalline soft magnetic materials.

Author Contributions: All authors contributed equally to this work. All authors have read and agreed to the published version of the manuscript.

Funding: This research received no external funding.

Acknowledgments: The review was made within the framework of state work No. FEUZ-0836-0020.

Conflicts of Interest: The authors declare no conflict of interest.

References

1. Yoshizawa, Y.; Yamauchi, K.; Oguma, S. Fe-Base Soft Magnetic Alloy and Method of Producing Same. U.S. Patent 4881989, 21 November 1989. Priority Japan 61-297838, 15 December 1986.
2. Yoshizawa, Y.; Oguma, S.; Yamauchi, K. New Fe-based soft magnetic alloys composed of ultrafine grain structure. *J. Appl. Phys.* **1988**, *64*, 6044–6046. [CrossRef]
3. Narasimhan, M.C. Continuous Casting Method for Metallic Strips. US Patent 4142571, 6 March 1979. Priority, 2 August 1977.
4. Luborsky, F.E.; Becker, J.J.; Walter, J.L.; Liebermann, H.H. Formation and magnetic properties of Fe-B-Si amorphous alloys. *IEEE Trans. Magn.* **1979**, *15*, 1146–1149. [CrossRef]
5. Swartz, J.C.; Haugh, J.J.; Krause, R.F.; Kossowsky, R. Coercivity effects of iron microcrystals in amorphous $Fe_{81}B_{13.5}Si_{3.5}C_2$. *J. Appl. Phys.* **1981**, *52*, 1908–1910. [CrossRef]
6. Ok, H.N.; Morrish, A.H. Origin of the perpendicular anisotropy in amorphous $Fe_{82}B_{12}Si_6$ ribbons. *Phys. Rev. B* **1981**, *23*, 2257–2261. [CrossRef]
7. Herzer, G.; Hilzinger, H.R. Surface crystallization and magnetic properties in amorphous iron rich alloys. *J. Magn. Magn. Mater.* **1986**, *62*, 143–151. [CrossRef]
8. Mager, A. Über den Einfluß der Korngröße auf die Koerzitivkraft. *Ann. Phys.* **1952**, *446*, 15–16. [CrossRef]
9. Herzer, G. Grain structure and magnetism of nanocrystalline ferromagnets. *IEEE Trans. Magn.* **1989**, *25*, 3327–3329. [CrossRef]
10. Herzer, G. The random anisotropy model. In *Properties and Applications of Nanocrystalline Alloys from Amorphous Precursors*; Idzikowski, B., Švec, P., Miglierini, M., Eds.; Springer: Dordrecht, The Netherlands, 2005; Volume 184, pp. 15–34. [CrossRef]
11. Herzer, G. Anisotropies in soft magnetic nanocrystalline alloys. *J. Magn. Magn. Mater.* **2005**, *294*, 99–106. [CrossRef]
12. Abo, G.S.; Hong, Y.-K.; Park, J.; Lee, J.; Lee, W.; Choi, B.-C. Definition of magnetic exchange length. *IEEE Trans. Magn.* **2013**, *49*, 4937–4939. [CrossRef]
13. Alben, R.; Becker, J.J.; Chi, M.C. Random anisotropy in amorphous ferromagnets. *J. Appl. Phys.* **1978**, *49*, 1653–1658. [CrossRef]
14. Herzer, G. Grain size dependence of coercivity and permeability in nanocrystalline ferromagnets. *IEEE Trans. Magn.* **1990**, *26*, 1397–1402. [CrossRef]
15. Herzer, G. Nanocrystalline soft magnetic alloys. In *Handbook of Magnetic Materials*; Buschow, K.H.J., Ed.; Elsevier: Amsterdam, The Netherlands, 1997; Volume 10, pp. 415–462.
16. Suzuku, K.; Herzer, G.; Cadogan, J.M. The effect of coherent uniaxial anisotropies on the grain-size dependence of coercivity in nanocrystalline soft magnetic alloys. *J. Magn. Magn. Mater.* **1998**, *177–181*, 949–951. [CrossRef]
17. Biyoh, T.; Makino, A.; Inoue, A. The effect of grain-size distribution on coercivity in nanocrystalline soft magnetic alloys. *J. Magn. Magn. Mater.* **2004**, *272–276*, 1445–1446. [CrossRef]
18. Bolyachkin, A.S.; Komogortsev, S.V. Power-law behavior of coercivity in nanocrystalline magnetic alloys with grain-size distribution. *Scr. Mater.* **2018**, *152*, 55–58. [CrossRef]
19. Starodubtsev, Y.N. *Physical Properties and Application of Soft Magnetic Materials*; Hotline–Telecom: Moscow, Russia, 2020.
20. Qin, J.; Gu, T.; Yang, L.; Bian, X. Study on structural relationship between the liquid and amorphous $Fe_{78}Si_9B_{13}$ alloys by *ab initio* molecular dynamics simulation. *Appl. Phys. Lett.* **2007**, *90*, 201909. [CrossRef]
21. Popel, P.S.; Sidorov, V.E. Microheterogeneity of liquid metallic solutions and its influence on the structure and properties of rapidly quenched alloys. *Mater. Sci. Eng. A* **1997**, *226–228*, 237–244. [CrossRef]
22. Konev, S.N.; Dovgopol, S.P.; Geld, P.V. Phase diagram of the Fe-B system in the melt. *Doklady Akademii Nauk SSSR* **1982**, *262*, 88–90.
23. Dong, B.S.; Zhou, S.X.; Wang, Y.G.; Li, Y.; Qin, J.Y.; Li, G.Z. Revealing a structure transition in typical Fe-based glass-forming alloy. *J. Non Cryst. Solids* **2018**, *498*, 305–308. [CrossRef]
24. Il'inskii, A.; Slyusarenko, S.; Slukhovskii, O.; Kaban, I.; Hoyer, W. Structural properties of liquid Fe-Si alloys. *J. Non Cryst. Solids* **2002**, *306*, 90–98. [CrossRef]
25. Bel'tyukov, A.L.; Lad'yanov, V.I.; Shishmarin, A.I. Viscosity of Fe-Si melts with silicon content up to 45 at%. *High Temp.* **2014**, *52*, 185–191. [CrossRef]
26. Zhou, S.; Dong, B.; Xiang, R.; Zhang, G.; Qin, J.; Bian, X. Influence of clusters in melt on subsequent glass-formation and crystallization of Fe-Si-B metallic glasses. *Prog. Nat. Sci. Mater.* **2015**, *25*, 137–140. [CrossRef]
27. Frenkel, J. *Kinetic Theory of Liquids*; Dover Publications: New York, NY, USA, 1955; pp. 188–223.

28. Baum, B.A. *Metal Liquids*; Nauka: Moscow, Russia, 1979; pp. 67–80.
29. Dahlborg, U.; Calvo-Dahlborg, M.; Popel, P.S.; Sidorov, V.E. Structure and properties of some glass-forming liquid alloys. *Eur. Phys. J. B* **2000**, *14*, 639–648. [CrossRef]
30. Bel'tyukov, A.L.; Goncharov, O.Y.; Lad'yanov, V.I. Features of polytherms of the viscosity of Fe-B melts. *Rus. J. Phys. Chem.* **2017**, *91*, 1919–1924. [CrossRef]
31. Dong, B.; Zhou, S.; Qin, J.; Li, Y.; Chen, H.; Wang, Y. The hidden disintegration of cluster heterogeneity in Fe-based glass-forming. *Prog. Nat. Sci. Mater.* **2018**, *28*, 696–703. [CrossRef]
32. Miettinen, J.; Visuri, V.-V.; Fabritius, T.; Milcheva, N.; Vassilev, G. Thermodynamic description of ternary Fe-B-Si systems. Part 5: Fe-B-Si. *Arch. Metall. Mater.* **2019**, *64*, 1239–1248. [CrossRef]
33. Lad'yanov, V.I.; Logunov, S.V.; Pakhomov, S.V. Oscillatory relaxation in nonequilibrium metallic melts at fast melting. *Rus. Metall. Met.* **1998**, *5*, 23–26.
34. Vasin, M.G.; Lad'yanov, V.I. Structural transitions and nonmonotonic relaxation processes in liquid metals. *Phys. Rev. E* **2003**, *68*, 051202. [CrossRef] [PubMed]
35. Zamyatin, V.M.; Baum, B.A.; Mezenin, A.A.; Shmakova, K.Y. Time dependences of the melt properties, their significance, features and options for explanation. *Rasplavy* **2010**, *5*, 19–31.
36. Tsepelev, V.; Starodubtsev, Y.; Konashkov, V.; Wu, K.; Wang, R. Melt viscosity of nanocrystalline alloys in the model of free volume. *J. Alloys Comp.* **2019**, *790*, 547–550. [CrossRef]
37. Greenwood, N.N.; Earnshaw, A. *Chemistry of the Elements*; Butterworth–Heinemann: Oxford, UK, 1998.
38. Oono, N.; Nitta, H.; Iijima, Y. Diffusion of niobium in α-iron. *Mater. Trans.* **2003**, *44*, 2078–2083. [CrossRef]
39. Bonny, G.; Castin, N.; Bullens, J.; Bakaev, A.; Klaver, T.C.P.; Terentyev, D. On the mobility of vacancy clusters in reduced activation steels: An atomistic study in the Fe-Cr-W model alloy. *J. Phys. Condens. Matter.* **2013**, *25*, 315401. [CrossRef] [PubMed]
40. Calvo-Dahlborg, M.; Popel, P.S.; Kramer, M.J.; Besser, M.; Morris, J.R.; Dahlborg, U. Superheat-dependent microstructure of molten Al-Si alloys of different compositions studied by small angle neutron scattering. *J. Alloys Comp.* **2013**, *550*, 9–22. [CrossRef]
41. Starodubtsev, Y.N.; Son, L.D.; Tsepelev, V.S.; Tyagunov, G.V.; Tishkin, A.P.; Korobka, O.B. Influence of the melt heating temperature on the mechanical and magnetic properties of an amorphous ribbon. *Rasplavy* **1992**, *4*, 76–79.
42. Manov, V.P.; Popel, S.I.; Buler, P.I.; Manukhin, A.B.; Komlev, D.G. The influence of quenching temperature on the structure and properties of amorphous alloys. *Mater. Sci. Eng. A* **1991**, *133*, 535–540. [CrossRef]
43. Tabachnikova, E.D.; Bengus, V.Z.; Egorov, D.V.; Tsepelev, V.S.; Ocelík, V. Mechanical properties of amorphous alloys ribbon prepared by rapid quenching of the melt after different thermal treatments before quenching. *Mater. Sci. Eng. A* **1997**, *226–228*, 887–890. [CrossRef]
44. Tsepelev, V.; Starodubtsev, Y.; Konashkov, V. Melt viscosity of the soft magnetic nanocrystalline $Fe_{72.5}Cu_1Nb_2Mo_{1.5}Si_{14}B_9$ alloy. *EPJ Web Conf.* **2017**, *151*, 040062017. [CrossRef]
45. Kochetkova, Y.A.; Starodubtsev, Y.N.; Tsepelev, V.S. Kinematic viscosity of melt prepared from an amorphous $Fe_{72.5}Cu_1Nb_2Mo_{1.5}Si_{14}B_9$ ribbon. In *IOP Conference Series: Materials Science and Engineering*; IOP Publishing: Bristol, UK, 2020; Volume 969, p. 012027. [CrossRef]
46. Batschinski, A.I. Untersuchungen über die innere Reibungen der Flüssigkeiten. *Z. Phys. Chem.* **1913**, *84*, 643–706. [CrossRef]
47. Glasstone, S.; Laidler, K.; Eyring, H. *The Theory of Rate Processes. The Kinetics of Chemical Reactions, Viscosity, Diffusion and Electrochemical Phenomena*; McGraw Hill: New York, NY, USA; London, UK, 1941; pp. 477–551.
48. Longuet-Higgins, H.C.; Pople, J.A. Transport properties of a dense fluid of hard spheres. *J. Chem. Phys.* **1956**, *25*, 884–889. [CrossRef]
49. Poole, C.P., Jr.; Owens, F.J. *Introduction to Nanotechnology*; John Wiley & Sons: Hoboken, NJ, USA, 2003; pp. 8–15.
50. Tsepelev, V.; Starodubtsev, Y.; Konashkov, V.; Belozerov, V. Thermomagnetic analysis of soft magnetic nanocrystalline alloys. *J. Alloys Comp.* **2017**, *707*, 210–213. [CrossRef]
51. Lyasotskii, I.V.; Dyakonova, N.B.; Vlasova, E.N.; Dyakonov, D.L.; Yazvitskii, M.Y. Metastable and quasiperiodic phases in rapidly quenched Fe-B-Si-Nb(Cu) alloys. *Phys. Stat. Sol. (a)* **2006**, *203*, 259–270. [CrossRef]
52. Pan, S.P.; Qin, J.Y.; Gu, T.K.; Yang, L.; Bian, X.F. Correlation between local structure of metals and glass forming ability for $Fe_{78}M_9B_{13}$ (M = Nb, Si, and Zr) alloys. *J. Appl. Phys.* **2009**, *105*, 013531. [CrossRef]
53. Tsepelev, V.S.; Starodubtsev, Y.N.; Wu, K.M.; Kochetkova, Y.A. Nanoparticles size in $Fe_{73.5}Cu_1Mo_3Si_{13.5}B_9$ melt. *Key Eng. Mater.* **2020**, *861*, 107–112. [CrossRef]
54. Hono, K.; Inoue, A.; Sakurai, T. Atom probe analysis of $Fe_{73.5}Si_{13.5}B_9Nb_3Cu_1$ nanocrystalline soft magnetic material. *Appl. Phys. Lett.* **1991**, *58*, 2180–2182. [CrossRef]
55. Hono, K.; Hiraga, K.; Wang, Q.; Inoue, A.; Sakurai, T. The microstructure evolution of a $Fe_{73.5}Si_{13.5}B_9Nb_3Cu_1$ nanocrystalline soft magnetic material. *Acta Metall. Mater.* **1992**, *40*, 2137–2147. [CrossRef]
56. Soisson, F.; Fu, C.-C. Cu-precipitation kinetics in α-Fe from atomistic simulations: Vacancy-trapping effects and Cu-cluster mobility. *Phys. Rev. B* **2007**, *76*, 214102. [CrossRef]
57. Müller, M.; Mattern, N.; Illgen, L. The influence of different Cu/Nb content on the structure and magnetic properties in nanocrystalline FeBSi base alloys. *J. Magn. Magn. Mater.* **1992**, *112*, 263–268. [CrossRef]
58. Lefebvre, W.; Morin-Grognet, S.; Danoix, F. Role of niobium in the nanocrystallization of a $Fe_{73.5}Si_{13.5}B_9Nb_3Cu$ alloy. *J. Magn. Magn. Mater.* **2006**, *301*, 343–351. [CrossRef]

59. Hono, K.; Ping, D.H.; Ohnuma, M.; Onodera, H. Cu clustering and Si portioning in the early crystallization stage of an $Fe_{73.5}Si_{13.5}B_9Nb_3Cu_1$ amorphous alloy. *Acta Mater.* **1999**, *47*, 997–1006. [CrossRef]
60. Danzig, A.; Mattern, N. Time-resolved X-ray diffraction studies on the crystallization of amorphous FeSiB-based alloys. *Phys. Stat. Sol. (a)* **1995**, *147*, 335–345. [CrossRef]
61. Nikul'chenkov, N.N.; Yurovskikh, A.S.; Starodubtsev, Y.N.; Lobanov, M.L. Phase and structural transformations in a nanocrystalline alloy $Fe_{72.5}Cu_1Nb_2Mo_{1.5}Si_{14}B_9$. *Lett. Mater.* **2019**, *9*, 64–69. [CrossRef]
62. Predel, B. Fe-Si (Iron-Silicon). In *Landolt—Börnstein, Group IV Physical Chemistry*; Springer: Berlin, Germany, 1995; Volume 5e, pp. 1–6. [CrossRef]
63. Tsepelev, V.S.; Starodubtsev, Y.N.; Wu, K.M.; Tsepeleva, N.P. Thermomagnetic analysis of the crystallization in soft magnetic nanocrystalline alloys. *Key Eng. Mater.* **2019**, *846*, 67–71. [CrossRef]
64. Tsepelev, V.; Konashkov, V.; Starodubtsev, Y.; Belozerov, V.; Gaipisherov, D. Optimum regime of heat treatment of soft magnetic amorphous materials. *IEEE Trans. Magn.* **2012**, *48*, 1327–1330. [CrossRef]
65. Tsepelev, V.S.; Starodubtsev, Y.N.; Zelenin, V.A.; Kataev, V.A.; Belozerov, V.Y.; Konashkov, V.V. Dilatometric analysis of the process the nanocrystallization of $Fe_{72.5}Cu_1Nb_2Mo_{1.5}Si_{14}B_9$ soft magnetic alloy. *Phys. Met. Metallogr.* **2017**, *118*, 553–557. [CrossRef]
66. Kubaschewski, O. *Iron—Binary Phase Diagrams*; Springer: Heidelberg, Germany, 1982; pp. 136–139.
67. Chien, C.L.; Musser, D.; Gyorgy, E.M.; Sherwood, R.C.; Chen, H.S.; Luborsky, F.E.; Walter, J.L. Magnetic properties of amorphous Fe_xB_{100-x} ($72 \leq x \leq 86$) and crystalline Fe_3B. *Phys. Rev. B* **1979**, *20*, 283–295. [CrossRef]
68. Jeffries, J.B.; Hershkowitz, N. Temperature dependence of the hyperfine interactions of FeB. *Phys. Lett. A* **1969**, *30*, 187–188. [CrossRef]
69. Barinov, V.A.; Voronin, V.I.; Surikov, V.T.; Kazantsev, V.A.; Tsurin, V.A.; Fedorenko, V.V.; Novikov, S.I. Structure and magnetic properties of metastable Fe-B phases. *Phys. Met. Metallogr.* **2005**, *100*, 456–467.
70. Chen, W.A.; Ryder, P.L. X-ray and differential scanning calorimetry study of the crystallization of amorphous $Fe_{73.5}Cu_1Nb_3Si_{13,5}B_9$ alloy. *Mater. Sci. Eng. B* **1995**, *34*, 204–209. [CrossRef]
71. Borrego, J.M.; Conde, C.F.; Conde, A. Thermomagnetic study of devitrification in Fe–Si–B–Cu–Nb(–X) alloys. *Phil. Mag. Lett.* **2000**, *80*, 359–365. [CrossRef]
72. Gerling, R.; Schimansky, F.P.; Wagner, R. Restoration of the ductility of thermally embrittled amorphous alloys under neutron-irradiation. *Acta Metall.* **1987**, *35*, 1001–1006. [CrossRef]
73. Niu, Y.C.; Bian, X.F.; Wang, W.M. Origin of ductile-brittle transition of amorphous $Fe_{78}Si_9B_{13}$ ribbon during low temperature annealing. *J. Non Cryst. Solids* **2004**, *341*, 40–45. [CrossRef]
74. Yoshizawa, Y.; Yamauchi, K. Magnetic properties of Fe-Cu-M-S-B (M = Cr, V, Nb, Ta, W) alloys. *Mater. Sci. Eng. A* **1991**, *133*, 176–179. [CrossRef]
75. Yamauchi, K.; Yoshizawa, Y. Recent development of nanocrystalline soft magnetic alloys. *Nanostruct. Mater.* **1995**, *6*, 247–254. [CrossRef]
76. Müller, M.; Mattern, N.; Kühn, U. Correlation between magnetic and structural properties of nanocrystalline soft magnetic alloys. *J. Magn. Magn. Mater.* **1996**, *157–158*, 209–210. [CrossRef]
77. Tsepelev, V.S.; Starodubtsev, Y.N.; Belozerov, V.Y. The effect of inhibitors on the structure and magnetic properties of nanocrystalline soft magnetic alloys. *Phys. Met. Metallogr.* **2018**, *119*, 831–836. [CrossRef]
78. Peña Rodríguez, V.A.; Flores Regalado, J.; Baggio-Saitovitch, E.; Passamani, E.C. Nanocrystallization process in Finemet-type alloys followed by in situ ^{57}Fe Mössbauer spectroscopy. *J. Alloys Comp.* **2004**, *379*, 23–27. [CrossRef]
79. Nakamura, Y. *Alloys and Compounds of d-Elements with Main Group Elements*; Landolt-Börnstein New Series, Group III; Part, C; Springer: Berlin, Germany, 1988; Volume 19, p. 26.
80. Müller, M.; Mattern, N. The influence of refractory element additions on the magnetic properties and on the crystallization behaviour of nanocrystalline soft magnetic Fe-B-S-Cu alloys. *J. Magn. Magn. Mater.* **1994**, *136*, 79–87. [CrossRef]
81. Mattern, N.; Müller, M.; Danzig, A.; Kühn, U. Influence of additions on the formation of nanocrystalline Fe_3Si by crystallization of amorphous $Fe_{76.5-x}B_7Si_{15.5}Cu_1R_x$. *Nanostruct. Mater.* **1995**, *6*, 625–628. [CrossRef]
82. Hume-Rothery, W.; Raynor, G.V. *The Structure of Metals and Alloys*; The Institute of Metals: London, UK, 1962; pp. 97–104.
83. Gottstein, G.; Shvindlerman, L.S. *Grain Boundary Migration in Metals: Thermodynamics, Kinetics, Applications*; CRC Press: Boca Raton, FL, USA; London, UK; New York, NY, USA, 2010; pp. 144–282.
84. Keylin, V.I.; Belozerov, V.Y.; Starodubtsev, Y.N. Magnetic Alloy for Oxidizing Annealing and Method for Production Thereof. RU Patent 2009358, 15 March 1994. Priority 20 April 1992.
85. Starodubtsev, Y.N.; Belozerov, V.Y. *Magnetic Properties of Amorphous and Nanocrystalline Alloys*; Ural University: Ekaterinburg, Russia, 2002.
86. Filippov, B.N.; Shulika, V.V.; Potapov, A.P.; Vil'danova, N.F. Magnetic properties and temperature stability of a molybdenum-doped finemet-type alloy. *Tech. Phys.* **2014**, *59*, 373–377. [CrossRef]
87. Lu, W.; Yan, B.; Li, Y.; Tang, R. Structure and soft magnetic properties of V-doped Finemet-type alloys. *J. Alloys Comp.* **2008**, *454*, L10–L13. [CrossRef]
88. Lu, W.; Fan, J.; Wang, Y.; Yan, B. Microstructure and magnetic properties of $Fe_{72.5}Cu_1M_2V_2Si_{13.5}B_9$ (M = Nb, Mo, (Nb,Mo), (MoW)) nanocrystalline alloys. *J. Magn. Magn. Mater.* **2010**, *322*, 2935–2937. [CrossRef]

89. Glazer, A.A.; Lukshina, V.A.; Potapov, A.P.; Noskova, N.I. Nanocrystalline alloy $Fe_{73.5}Cu_1Nb_3Si_{13.5}B_9$ prepared from amorphous state by quick crystallization at elevated temperatures. *Fiz. Met. Metalloved.* **1992**, *8*, 96–100.
90. Chikazumi, S. *Physics of Ferromagnetism*; Oxford University Press: New York, NY, USA, 1997.
91. Walz, F.; Deusch, H.; Kronmüller, H. Investigation of magnetic after-effect in magnetite near Verwey temperature. *Phys. Stat. Sol. (a)* **1979**, *53*, 519–528. [CrossRef]
92. Gong, M.M.; Liu, F.; Zhang, K. Thermodynamic stability of binary nanocrystalline alloys: Analysis of solute and excess vacancy. *Appl. Phys. A* **2011**, *105*, 927–934. [CrossRef]
93. Tsepelev, V.S.; Starodubtsev, Y.N.; Belozerov, V.Y. Thermal stability of nanocrystalline soft magnetic alloys with different inhibitors. *Key Eng. Mater.* **2019**, *821*, 250–255. [CrossRef]
94. Starodubtsev, Y.N.; Tsepelev, V.S. Analysis of losses in soft magnetic nanocrystalline alloys as a function of induction and frequency. *J. Magn. Magn. Mater.* **2020**, *500*, 166347. [CrossRef]
95. Kedous-Lebouc, A.; Brissonneau, P. Accelerated aging behavior under a compressive stress of Metglas 2605S2 amorphous ribbons. *Phys. Scr.* **1989**, *39*, 112–114. [CrossRef]
96. Kataev, V.A.; Starodubtsev, Y.N.; Mineev, F.V. Concerning the magnetic losses in annealed ribbons of amorphous alloy $Fe_{81}B_{13}Si_4C_2$. *Phys. Met. Metallogr.* **1990**, *70*, 199–202.
97. Narita, K.; Enokizono, M. Effect of ordering on magnetic properties of 6.5-percent silicon-iron alloy. *IEEE Trans. Magn.* **1979**, *15*, 911–915. [CrossRef]
98. Herzer, G. Magnetic field-induced anisotropy in nanocrystalline Fe-Cu-Nb-Si-B alloys. *J. Magn. Magn. Mater.* **1994**, *133*, 248–250. [CrossRef]
99. Schäfer, R. The magnetic microstructure of nanostructured materials. In *Nanoscale Magnetic Materials and Applications*; Liu, J., Fullerton, E., Gutfleisch, O., Sellmyer, D., Eds.; Springer: Boston, MA, USA, 2009; pp. 275–307. [CrossRef]
100. Starodubtsev, Y.N.; Kataev, V.A.; Bessonova, K.O.; Tsepelev, V.S. Hysteresis losses in nanocrystalline alloys with magnetic-field-induced anisotropy. *J. Magn. Magn. Mater.* **2019**, *479*, 19–26. [CrossRef]
101. Sixtus, K. Anisotropie in Eisen-Silizium-Einkristallen nach Glühen im Magnetfeld. *Z. Angew. Phys.* **1970**, *28*, 270–274.
102. Forsch, K. Diffusionsanisotropie in Eisen–Silizium-Legierungen. *Phys. Stat. Sol. (b)* **1970**, *42*, 329–344. [CrossRef]
103. Dennler, S.; Hafner, J. First-principles study of lattice dynamics and diffusion in DO_3-type Fe_3Si. *Phys. Rev. B* **2006**, *73*, 174303. [CrossRef]
104. Madugundo, R.; Geoffroy, O.; Waeckerle, T.; Frincu, B.; Kodjikian, S.; Rivoirard, S. Inproved soft magnetic properties in nanocrystalline FeCuNbSiB Nanophy® cores by intense magnetic field annealing. *J. Magn. Magn. Mater.* **2017**, *422*, 475–478. [CrossRef]
105. Glazer, A.A.; Kleinerman, N.M.; Lukshina, V.A.; Potapov, A.P.; Serikov, V.V. Thermomechanical treatment of the nanocrystalline alloy $Fe_{73.5}Cu_1Nb_3Si_{13.5}B_9$. *Phys. Met. Metallogr.* **1991**, *72*, 53–58.
106. Herzer, G.; Budinsky, V.; Polak, C. Magnetic properties of nanocrystalline FeCuNbSiB with huge creep induced anisotropy. In *Journal of Physics: Conference Series*; IOP Publishing: Bristol, UK, 2011; Volume 266, p. 012010. [CrossRef]
107. Serikov, V.V.; Kleinerman, N.M.; Volkova, E.G.; Lukshina, V.A.; Potapov, A.P.; Svalov, A.V. Structure and magnetic properties of nanocrystalline FeCuNbSiB alloys after a thermomechanical treatment. *Phys. Met. Matallogr.* **2006**, *102*, 268–273. [CrossRef]
108. Ohnuma, M.; Hono, K.; Yanai, T.; Fukunaga, H.; Yoshizawa, Y. Direct evidence for structural origin of stress-induced magnetic anisotropy in Fe-Si-B-Nb-Cu nanocrystalline alloys. *Appl. Phys. Lett.* **2003**, *83*, 2859–2861. [CrossRef]
109. Yoshizawa, Y.; Fujii, S.; Ping, D.H.; Ohnuma, M.; Hono, K. Magnetic properties of nanocrystalline FeMCuNbSiB alloys (M: Co, Ni). *Scr. Mater.* **2003**, *48*, 863–868. [CrossRef]
110. Kataev, V.A.; Starodubtsev, Y.N.; Mikhalitsyna, E.A.; Belozerov, V.Y.; Tsyngalov, R.V. Magnetic properties and induced anisotropy of nanocrystalline $Fe_{72.5-x}Ni_xCu_{1.1}Nb_{1.9}Mo_{1.5}Si_{14.3}B_{8.7}$ alloys. *Phys. Met. Metallogr.* **2017**, *118*, 558–563. [CrossRef]
111. Tsepelev, V.S.; Starodubtsev, Y.N.; Wu, K.M. Influence of Ni on crystallization and magnetic properties of $Fe_{72.5-x}Ni_xCu_{1.1}Nb_2Mo_{1.5}Si_{14}B_9$ alloys. *J. Cryst. Growth* **2019**, *528*, 125256. [CrossRef]
112. Swartzendruber, L.J.; Itkin, V.P.; Alcock, C.B. The Fe-Ni (iron-nickel) system. *J. Phase Equiliria* **1991**, *12*, 288–312. [CrossRef]
113. Agudo, P.; Vázquez, M. Influence of Ni on the structural and magnetic properties of $Ni_xFe_{73.5-x}Si1_{3.5}B_9Nb_3Cu_1$ ($0 \leq x \leq 25$) alloys. *J. Appl. Phys.* **2005**, *97*, 023901. [CrossRef]
114. Lukshina, V.A.; Dmitrieva, N.V.; Volkova, E.G.; Shishkin, D.A. Magnetic properties of the $Fe_{63.5}Ni_{10}Cu_1Nb_3Si_{13.5}B_9$ alloy nanocrystallized in the presence of tensile stresses. *Phys. Met. Metallogr.* **2019**, *120*, 320–324. [CrossRef]
115. Wakiyama, T.; Takahashi, M.; Nishimaki, S.; Shimoda, J. Magnetic properties of Fe-Si-Al single crystals. *IEEE Trans. Magn.* **1981**, *17*, 3147–3150. [CrossRef]
116. Tate, B.J.; Parmar, B.S.; Todd, I.; Davies, H.A.; Gibbs, M.R.J.; Major, R.V. Soft magnetic properties and structures of nanocrystalline Fe-Al-Si-B-Cu-Nb alloys ribbons. *J. Appl. Phys.* **1998**, *83*, 6335–6337. [CrossRef]
117. Mushnikov, N.V.; Potapov, A.P.; Shishkin, D.A.; Protasov, A.V.; Golovnya, O.A.; Shchegoleva, N.N.; Gaviko, V.S.; Shunyaev, K.Y.; Bykov, V.A.; Starodubtsev, Y.N.; et al. Magnetic properties and structure of nanocrystalline FINEMET alloys with various iron contents. *Phys. Met. Metallogr.* **2015**, *116*, 663–670. [CrossRef]
118. Sizuki, K.; Makino, A.; Inoue, A.; Masumoto, T. Soft magnetic properties of nanocrystalline bcc Fe-Zr-B and Fe-M-B-Cu (M = transition metal) alloys with high saturation magnetization. *J. Appl. Phys.* **1991**, *70*, 6232–6237. [CrossRef]

119. Makino, A.; Kubota, T.; Yubuta, K.; Inoue, A.; Urata, A. Low core losses and magnetic properties of $Fe_{85-86}Si_{1-2}B_8P_4Cu_1$ nanocrystalline alloys with high B for power applications. *J. Appl. Phys.* **2011**, *109*, 07A302. [CrossRef]
120. Matsuura, M.; Zhang, Y.; Nishijima, M.; Makino, A. Role of P in nanocrystallization of $Fe_{85}Si_2B_8P_4Cu_1$. *IEEE Trans. Magn.* **2014**, *50*, 2003304. [CrossRef]
121. Ohta, M.; Yoshizawa, Y. Magnetic properties of high-B_s Fe-Cu-Si-B nanocrystalline soft magnetic alloys. *J. Magn. Magn. Mater.* **2008**, *320*, e750–e753. [CrossRef]
122. Suzuki, K.; Parsons, R.; Zgang, B.; Onodera, K.; Kishimoto, H.; Shoji, T.; Kato, A. Nanocrystalline soft magnetic materials from binary alloy precursors with high saturation magnetization. *AIP Adv.* **2019**, *9*, 035311. [CrossRef]
123. Makino, A.; Inoue, A.; Masumoto, T. Soft magnetic properties of nanocrystalline Fe-M-B (M = Zr, Hf, Nb) alloys with high magnetization. *Nanostruct. Mater.* **1995**, *6*, 985–988. [CrossRef]
124. Pradeep, K.G.; Herzer, G.; Choi, P.; Raabe, D. Atom probe tomography study of ultrahigh nanocrystallization rates in FeSiNbBCu soft magnetic amorphous alloys on rapid annealing. *Acta Mater.* **2014**, *68*, 295–309. [CrossRef]
125. Suzuki, K.; Herzer, G. Magnetic-field-induced anisotropies and exchange softening in Fe-rich nanocrystalline soft magnetic alloys. *Scr. Mater.* **2013**, *67*, 548–553. [CrossRef]
126. Pry, R.H.; Bean, C.P. Calculation of the loss in magnetic sheet materials using a domain model. *J. Appl. Phys.* **1958**, *29*, 532–533. [CrossRef]
127. Flohrer, S.; Schäfer, R.; Herzer, G. Magnetic microstructure of nanocrystalline FeCuNbSiB soft magnets. *J. Non Cryst. Sol.* **2008**, *354*, 5097–5100. [CrossRef]
128. Kataev, V.A.; Starodubtsev, Y.N.; Bessonova, K.O. Magnetizing of Finemet-type alloys by magnetization rotation in weak fields. In *Journal of Physics: Conference Series*; IOP Publishing: Bristol, UK, 2019; Volume 1389, p. 012120. [CrossRef]
129. Starodubtsev, Y.N.; Kataev, V.A.; Tsepelev, V.S. Dimension quantities of hysteresis loops. *J. Mag. Mag. Mater.* **2018**, *460*, 146–152. [CrossRef]
130. Starodubtsev, Y.N.; Kataev, V.A.; Bessonova, K.O.; Tsepelev, V.S. Interrelation of hysteresis characteristics of a soft magnetic nanocrystalline alloy. *Phys. Met. Metallogr.* **2019**, *120*, 121–127. [CrossRef]
131. Steinmetz, C.P. On the law of hysteresis. *Proc. IEEE* **1892**, *72*, 197–221, reprinted from *Amer. Inst. Electr. Eng. Trans.* **1892**, *9*, 3–64. [CrossRef]
132. Haller, T.R.; Kramer, J.J. Model for reverse-domain nucleation in ferromagnetic conductors. *J. Appl. Phys.* **1970**, *41*, 1036–1037. [CrossRef]
133. Flohrer, S.; Schäfer, R.; Polak, C.; Herzer, G. Interplay in uniform and random anisotropy in nanocrystalline soft magnetic alloys. *Acta Mater.* **2005**, *53*, 2937–2942. [CrossRef]
134. Flohrer, S.; Schäfer, R.; McCord, J.; Roth, S.; Schultz, L.; Herzer, G. Magnetization loss and domain refinement in nanocrystalline tape wound cores. *Acta Mater.* **2006**, *54*, 3253–3259. [CrossRef]
135. Flohrer, S.; Schäfer, R.; McCord, J.; Roth, S.; Schultz, L.; Fiorillo, F.; Günter, W.; Herzer, G. Dynamic magnetization process of nanocrystalline tape wound cores with transverse field-induced anisotropy. *Acta Mater.* **2006**, *54*, 4693–4698. [CrossRef]
136. Tsepelev, V.; Starodubtsev, Y.; Zelenin, V.; Belozerov, V.; Konashkov, V. Temperature affecting the magnetic properties of the $Co_{79-x}Fe_3Cr_3Si_{15}B_x$ amorphous alloy. *J. Alloys Comp.* **2015**, *643*, S280–S282. [CrossRef]
137. Yoshizawa, Y. Nanocrystalline soft magnetic materials and their applications. In *Handbook of Advanced Magnetic Materials*; Liu, Y., Sellmyer, D.J., Shindo, D., Eds.; Springer: Boston, MA, USA, 2006; pp. 124–158. [CrossRef]
138. Hilzinger, R.; Rodewald, W. *Magnetic Materials: Fundamentals, Product, Properties, Applications*; Publicis MCD: Erlangen, Germany, 2013; pp. 467–520.
139. Starodubtsev, Y.N. *Theory and Calculation of Low Power Transformers*, 3rd ed.; RadioSoft: Moscow, Russia, 2015; pp. 146–165.
140. Starodubtsev, Y. DC bias electrical reactor. *Silov. Elektron.* **2009**, *5*, 20–22.